International Journal of Heat and Mass Transfer 123 (2018) 172–191

Contents lists available at ScienceDirect

International Journal of Heat and Mass Transfer

journal homepage: www.elsevier.com/locate/ijhmt

Investigation of subcooled and saturated boiling heat transfer mechanisms, instabilities, and transient flow regime maps for large length-to-diameter ratio micro-channel heat sinks

Seunghyun Lee, V.S. Devahdhanush, Issam Mudawar *

Boiling and Two-Phase Flow Laboratory (PU-BTPFL), School of Mechanical Engineering, Purdue University, 585 Purdue Mall, West Lafayette, IN 47907, USA

ARTICLE INFO

Article history:
Received 29 September 2017
Received in revised form 31 January 2018
Accepted 5 February 2018
Available online 20 March 2018

Keywords:
Micro-channel
Subcooled flow boiling
Saturated flow boiling
Two-phase heat sink
Two-phase instabilities
Dryout

ABSTRACT

This study investigates the interfacial behavior and heat transfer mechanisms associated with flow boiling of R-134a in a micro-channel test module. The test module features 100 of 1 × 1 mm^2 square micro-channels. Large length of micro-channels used (609.6 mm) is especially important to capturing broad axial variations of both flow and heat transfer behavior. The fluid is supplied to the test module in subcooled state to enable assessment of both the subcooled boiling and saturated boiling regions. The study employs a combination of temperature measurements along the test module and high-speed video to explore crucial details of the flow, including dominant flow regimes, flow instabilities, and downstream dryout effects. It is shown that, unlike macro-channel flows, where flow regimes can be clearly demarcated, flow regimes in micro-channels are associated with transient fluctuations that are induced by flow instabilities. The dominant flow behavior and associated dryout effects are characterized with the aid of a new transient flow regime map and a dryout map, respectively. Two sub-regions of the subcooled boiling region, partially developed boiling (PDB) and fully developed boiling (FDB), are examined relative to dominant interfacial and heat transfer mechanisms, and a previous correlation is identified for accurate prediction of the heat transfer coefficient for both PDB and FDB. The saturated boiling region is shown to consist of three separate sub-regions: nucleate boiling dominated for qualities below 0.3, combined nucleate and convective boiling for qualities between 0.3 and 0.5, and convective boiling dominated for qualities above 0.5. Above 0.5, dryout effects begin to take effect, causing a gradual decline in the heat transfer coefficient followed downstream by a more severe decline. A previous correlation is identified for prediction of the heat transfer coefficient in the saturated boiling region.

1. Introduction

1.1. Two-phase cooling potential and features of two-phase mini/micro-channel cooling

Rapid escalation in heat dissipation in modern electronics and power applications, coupled with a quest for smaller and more lightweight packaging, has created a pressing need for more effective cooling solutions. Despite many innovative improvements to both air and single-phase liquid cooling, these cooling schemes have largely fallen short of maintaining acceptable device temperatures. These shortcomings have shifted interest among thermal system designers to two-phase cooling schemes, which capitalize on the coolant's both sensible and latent heat to greatly enhance cooling performance compared to single-phase cooling schemes [1].

Over the past three decades, investigators at the Purdue University Boiling and Two-Phase Flow Laboratory (PU-BTPFL) and several other researcher groups have examined a broad variety of two-phase cooling solutions, the most basic of which are capillary-driven devices (heat pipes, capillary pumped loops, and loop heat pipes) [2–4] and pool boiling thermosyphons [5–7]. For applications demanding more superior cooling performance, a variety of pump-driven schemes have also been proposed, including falling film [8,9], channel flow boiling [10,11], mini/micro-channel flow boiling [12–15], jet-impingement [16–19], and spray [20–26].

Of the different two-phase cooling schemes, those employing mini/micro-channel cooling have received particular attention because of a number of thermal and system attributes. Their key

* Corresponding author.
E-mail address: mudawar@ecn.purdue.edu (I. Mudawar).
URL: https://engineering.purdue.edu/BTPFL (I. Mudawar).

https://doi.org/10.1016/j.ijheatmasstransfer.2018.02.020
0017-9310/

Nomenclature

A_{base}	total base area of heat sink
Bo	boiling number, $Bo = (q''_H/Gh_{fg})$
C	empirical coefficient
c_p	specific heat at constant pressure
D_b	bubble detachment diameter
D_h	hydraulic diameter
G	mass velocity
g	gravitational acceleration
G_c	critical mass velocity
h	enthalpy; heat transfer coefficient
$\bar{h}$	average heat transfer coefficient
H_{ch}	micro-channel height
h_{fg}	latent heat of vaporization
h_{sub}	enthalpy of subcooling, $h_{sub} = h_{sat} - h$
H_{tc}	distance between thermocouple and bottom wall of micro-channel
j	superficial velocity
Ja^*	modified Jakob number, $Ja^* = c_{p,f}\Delta T_{sub,in}/h_{fg}$
$j_{g,cor}$	superficial velocity of vapor corrected relative to air
k	thermal conductivity
k_s	thermal conductivity of solid
L_{ch}	micro-channel length
L_{sp}	length of single-phase region
m	fin parameter; empirical exponent
$\dot{m}$	total mass flow rate of heat sink
MAE	mean absolute error (%)
n	empirical exponent
Nu	Nusselt number
N_{pch}	phase change number
N_{sub}	subcooling number
p	pressure
Pr	Prandtl number
q''	heat flux
q^*	dimensionless heat flux
q_B''	heat flux based on total base area of heat sink
q_H''	heat flux based on heated area of micro-channel
Re	Reynolds number
Su	Suratman number
T	temperature
t	time
$T_{b,f}$	bulk liquid temperature
T_w	micro-channel wall temperature
$T_{w,b}$	bottom wall temperature of micro-channel
v	specific volume
V_b	bulk fluid velocity
v_{fg}	specific volume difference between vapor and liquid
W_{ch}	micro-channel width
We	Weber number
We^*	modified Weber number
W_w	half-width of copper sidewall separating micro-channels
x	vapor quality
x_e	thermodynamic equilibrium quality
X_{tt}	turbulent-turbulent Lockhart-Martinelli parameter
z	axial coordinate

Greek symbols

α	void fraction
β	channel aspect ratio
η	fin efficiency
θ	percentage predicted within ±30%
μ	dynamic viscosity
ν	kinematic viscosity
ξ	percentage predicted within ±50%
ρ	density
σ	surface tension
ψ	dimensionless heat transfer rate
ψ_0	dimensionless heat transfer rate corresponding to $x_e = 0$

Subscripts

3	three-sided heating
4	four-sided heating
avg	average
b	bottom of micro-channel
cor	correlation for uniform circumferential (circular or four-sided) heating
devel	developing flow
exp	experimental
f	liquid
g	vapor
in	micro-channel inlet
k	liquid (f) or vapor (g)
lam	laminar flow
max	maximum
out	micro-channel outlet
pred	predicted
sat	saturation
sc	subcooled boiling
sp	single phase
sub	subcooling
tc	thermocouple
turb	turbulent flow
w	micro-channel wall
z	local properties along axial direction

thermal advantage is the ability to dissipate fairly high heat fluxes while maintaining relatively low device temperatures [27]. They are also very compact and lightweight, and require low flow rates and minimal coolant inventory. Other lesser known advantages are their versatility, including adaptability to pump-free loops [28,29], and flexibility of incorporation into hybrid cooling modules that combine the merits of mini/micro-channel flow boiling with those of jet impingement [30–32].

However, two-phase mini/micro-channel heat sinks also pose several challenges. Most of these challenges are associated with the use of small hydraulic diameter to enhance the two-phase heat transfer coefficient. For a given coolant flow rate, small hydraulic diameters are generally associated with high pressure drop. This may lead to appreciable compressibility, which results from large variations in specific volumes of the vapor and liquid with axially decreasing pressure. Another concern is increased flashing, which is the result of large variations in enthalpies of the vapor and liquid with axially decreasing pressure. For high mass velocities, the combined effects of compressibility and flashing increase the likelihood of two-phase choking, which is reflected in the following relation for critical mass velocity corresponding to a two-phase Mach number equal to unity [33].

$$G_c = \left\{ -\left[x\frac{dv_g}{dp} + (1-x)\frac{dv_f}{dp} - \frac{v_{fg}}{h_{fg}}\left(\frac{dh_f}{dp} + x\frac{dh_{fg}}{dp}\right)\right]\right\}^{-0.5}. \quad (1)$$

These concerns were first addressed by Bowers and Mudawar [34], who compared cooling performances of two heat sinks, one featuring 2.5-mm mini-channels and the other 0.51-mm micro-channels, using R-113 as working fluid. They showed that, while

both heat sinks produced fairly similar cooling performances, the micro-channel heat sink showed significantly higher pressure drop, resulting in appreciable compressibility and flashing, and high two-phase Mach number. Another concern with micro-channel heat sinks is occurrence of various forms of two-phase instabilities, including density-wave oscillations, parallel-channel instability, and severe pressure-drop oscillation [15,35]. And, while the latter, most severe instability, can be eliminated by throttling the flow upstream of the heat sink, density-wave oscillations and parallel-channel instabilities cannot be fully eliminated, but can be tolerated for most operating conditions.

1.2. Importance of two-phase micro-channel cooling to thermal management of space vehicles and planetary habitat, and need for large length-to-diameter micro-channel heat sinks

Following the Apollo manned missions to the Moon in the 1960s and 1970s, interest gradually shifted to manned missions to Mars and asteroids, and development of Martian habitat. These missions pose significant new design challenges resulting from greatly increased mission scope, complexity, and duration. These challenges are also reflected in unprecedented increases in both power requirements and heat dissipation demands.

A key research need that is crucial to future space missions is reducing the mass and volume of all future space vehicle subsystems. The present study concerns the Thermal Control System (TCS), which is tasked with controlling the temperature and humidity of the operating environment inside the space vehicle. Unlike single-phase liquid TCS technologies that rely exclusively on sensible heat rise of the working fluid to remove the heat from both avionics and crew, it is widely acknowledged that two-phase evaporators can greatly decrease TCS mass and volume with their ability to achieve orders of magnitude enhancement in heat transfer performance [36–42]. Among the various TCS evaporator designs being considered, micro-channel heat sinks are a prime contender, given their unusually large ratio of heat dissipation to TCS mass [43,44]. Implementing two-phase heat sinks in future space missions is a key motivation for the present study.

It is important to emphasize that, unlike the miniature two-phase heat sinks widely employed in the electronics industry, two-phase evaporators for future space systems are expected to require channels with comparatively large length-to-diameter ratio, and multiple parallel channels. Two important applications of micro-channel evaporators onboard space vehicles are ‘cold plates’ that are used to cool the avionics, and evaporators used to remove metabolic heat dissipated by the crew.

The vast majority of prior large length-to-diameter two-phase micro-channel studies have been focused on single channels [45–50]. This type of channel features appreciable axial variations in flow pattern, in many instances encountering the full range of patterns, namely bubbly, slug, churn, and annular, as well as different heat transfer mechanisms.

1.3. Subcooled flow boiling ($x_e < 0$)

Cooling of electronic and power devices is typically achieved by supplying the coolant to the micro-channels in subcooled state. This strategy allows the thermal management system to capitalize upon the coolant’s both sensible and latent heat, as well as delay critical heat flux (CHF) occurrence. Subcooled flow boiling is generally associated with appreciable thermal non-equilibrium across the flow area in terms of both fluid temperature and void fraction, and consists of two distinct sub-regions: *partially developed boiling* (PDB) and *fully developed boiling* (FDB). Fig. 1 shows the upstream PDB region is initiated with a finite, albeit small increase in void fraction from zero value initiated at the onset of nucleate boiling

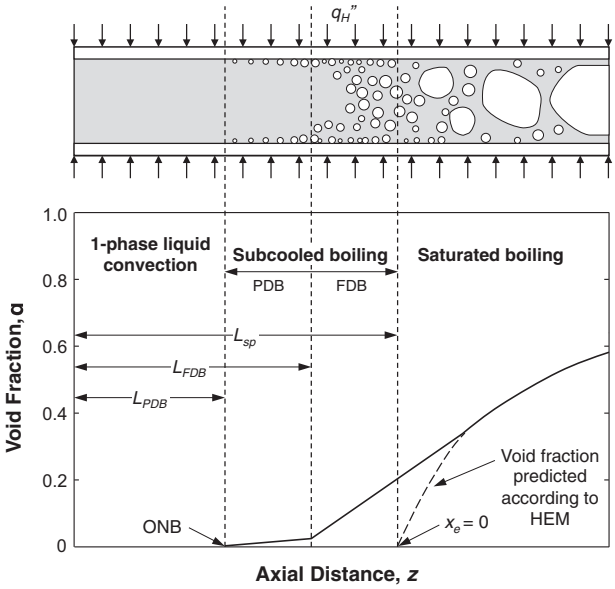

Fig. 1. Void fraction variations associated with partially developed boiling (PDB) and fully developed boiling (FDB) sub-regions of subcooled boiling, and with saturated boiling.

(ONB). The lack of any significant increase in void fraction is the result of appreciable condensation within the PDB region. Entering the FDB region, comparatively weaker condensation in the now warmer bulk fluid allows the void fraction to begin increasing more rapidly along the channel. Superimposed in Fig. 1 is the axial variation of void fraction predicted according to the Homogeneous Equilibrium Model (HEM), starting with zero value corresponding to $x_e = 0$, the transition point between the subcooled boiling and saturated boiling regions. Notice how lack of thermodynamic equilibrium causes the void fraction to begin increasing upstream of the $x_e = 0$ location, however, the actual void fraction variation tends to merge downstream with the variation predicted according to HEM.

Predictions of the wall temperature and heat flux corresponding to ONB have been investigated analytically by several investigators [51–54]. In an early treatment, Hsu and Graham [51] proposed a theoretical model that compared the superheat required to grow a bubble beyond the mouth of a surface cavity to the amount of superheat actually available in the near-wall liquid boundary layer. This model showed cavities of a radius that is dictated by tangency between required and available superheat curves are the first to nucleate; this model showed good agreement with Hsu and Graham’s own experimental data [52]. One disadvantage of this model is that it is not intended for low contact angle fluids. Also, use of a linear temperature profile in the near-wall liquid layer may not be applicable to all flow boiling situations. Sato and Matsumura [53] developed an analytic model that does not use contact angle or thermal layer thickness information. Davies and Anderson [54] modified an earlier analytical model by Bergles and Rohsenow [55] to account for contact angle and cavity size, which are dictated by working fluid and surface finish.

While Sato and Matsumura’s correlation has been widely used to predict ONB in macro-channels, Qu and Mudawar [56] proved experimentally that ONB in micro-channels is fundamentally different from that in macro-channels. They formulated a theoretical model that included both mechanical and thermal criteria for bubble growth and removal, which showed excellent agreement with their experimental data. Peng and Wang analyzed nucleation in micro-channels by using thermodynamic phase stability theory and theoretically predicted ONB in micro-channels [57],

concluding that both heat flux and wall temperature corresponding to ONB are greater for micro-channels than for macro-channels. A later study by Martin-Callizo et al. [58] also showed experimentally that the wall superheat corresponding to ONB is higher for a micro-channel than a macro-channel.

Transition from PDB to FDB in subcooled flow boiling in macro-channels has been examined by several investigators [55,59–62]. Bowring [60] noted that wall heat flux in the PDB region can be expressed as the sum of single-phase convection and nucleate boiling portions. They suggested the transition point between PDB and FDB occurs at the point of intersection between the single-phase and fully-developed boiling curves. Shah [61] used three dimensionless parameters (boiling number in addition to heat flux and subcooling parameters) to successfully predict his own data for different fluids.

Studies have also been performed to investigate heat transfer performance within the subcooled boiling region in micro-channels. Martin-Callizo et al. [58] examined subcooled flow boiling of R134a in vertical micro-channels and showed that higher inlet subcooling and smaller diameter increase the boiling heat transfer coefficient. Lee and Mudawar [14,15,63] showed that very high inlet subcooling (up to 93.59 °C) greatly enhances cooling performance for HFE7100 in micro-channels.

1.4. Saturated flow boiling ($x_e > 0$)

Recent micro-channel studies [46,47,64,65] suggest that heat transfer in the saturated flow boiling region can be categorized into two fundamentally different mechanisms: *nucleate boiling* and *convective boiling*, which are dominant in low and high quality regions of the channel, respectively. The nucleate boiling region is associated with high heat transfer coefficients and dominated by strong isolated bubble nucleation effects. However, the heat transfer coefficient begins to decrease as significant bubble coalescence begins to take effect. The nucleate boiling mechanism is encountered mostly in the bubbly and slug flow regions of the channel. The convective boiling region is associated with heat transfer across the liquid film in the annular flow region of the channel.

Saturated flow boiling experiments in a single long micro-channel have been conducted using a variety of fluids and channel geometries [45–48,66]. These studies showed the nucleate boiling mechanism is dominant for $x_e \leq 0.4$, where the heat transfer coefficient depends mostly on the heat flux, independent of mass velocity. On the other hand, the convective boiling mechanism is dominant for $x_e \geq 0.5$, where the heat transfer coefficient is influenced mostly by mass velocity and quality, independent of heat flux. The same studies suggest both mechanisms can occur concurrently for $0.3 \leq x_e \leq 0.6$.

Similar heat transfer coefficient trends have been observed in multi-channel heat sinks [67–70]. However, flow in multi-channel heat sinks is complicated by a variety of two-phase instabilities [64,65,71], some inducing vapor backflow to the inlet plenum [14,65,72,73], and intermittent dryout [64,65,73].

It is important to note that most published micro-channel studies concern short channels [67,68,70,74,75], which preclude the ability to capture detailed axial variations of two-phase flow regimes, dominant heat transfer mechanisms, flow instabilities, and dryout effects.

1.5. Objectives of study

The present study is part of a series of joint investigations between the Purdue University Boiling and Two-Phase Flow Laboratory (PU-BTPFL) and the NASA Glenn Research Center (GRC) whose ultimate goal is to develop two-phase thermal management design tools for future space vehicles.

Investigated in this study are two-phase heat transfer characteristics of a large length-to-diameter ratio multi micro-channel heat sink using a pumped two-phase loop. The long micro-channels in the heat sink enable detailed capture of axial variations of flow patterns and heat transfer coefficient, as well as both instability and dryout mechanisms, using both heat transfer measurements and high speed video motion analysis.

2. Experimental methods

2.1. Two-phase flow loop

Fig. 2(a) shows a schematic diagram of the R-134a two-phase flow loop that is used in the present study to regulate the coolant's operating conditions at the inlet to a large length-to-diameter ratio multi micro-channel test module. The fluid is circulated through the loop with the aid of a gear pump unit, composed of Micropump head and AC motor, and the flow rate measured downstream of the pump by a turbine flow meter. The coolant then passes through a throttling valve before entering the test module. The throttling valve plays the dual role of regulating pressure and flow rate, and preventing large pressure drop oscillations across the test module. The two-phase mixture exiting the test module is passed through an air-cooled condenser to bring the fluid to liquid state. A constant pressure junction in the flow loop is maintained downstream of the condenser with the aid of reservoir fitted with both a modular cooler and a PID-controlled heater. To achieve subcooled conditions at the inlet to the test module, the flow downstream of the constant pressure junction is routed through a plate-type heat exchanger that is connected to another modular subcooler. The subcooler also serves the purpose of preventing any cavitation in the gear pump. Fig. 2(b) shows images of the entire test facility, condenser, control console, and test module.

2.2. Micro-channel test module

The main component of the test module is a copper heat sink having a 609.6-mm long by 203.2-mm wide base area, and whose surface contains 100 of 1×1 mm^2 micro-channels. A recent paper by the present authors investigated different length-to-diameter ratio heat sinks from prior studies [73]. A general category of micro-channel heat sinks designated as having 'large' length-to-diameter ratio featured different flow patterns (bubbly to annular) and heat transfer mechanisms (nucleate to convective) concurrently along the axial direction. This categorization is achieved in the present study with L/d = 609.6. However, more comprehensive investigation of heat sink L/d ratio is warranted to arrive at a more systematic categorization into 'small', 'medium' and 'large' length-to-diameter ratio channels.

As shown in Fig. 3(b), the different layers of the test module are pressed together with the aid of a stainless steel support brace plate and a series of aluminum support bars atop, and another series of aluminum support bars below.

Further details concerning flow loop operation and test module construction are available in earlier studies by the authors [73,76].

2.3. Instrumentation and measurement accuracy

Video capture of the boiling flow is made possible through the test module's transparent cover plate with the aid of a Photron Ultima APX high-speed camera fitted with 105-mm Nikkor lens, with lighting provided by a fiber optic source. While the video camera is capable of shutter speeds as high as 1/200,000 s, good resolution and a reasonably wide field of view are achieved with a shutter speed of 1/8000 s.

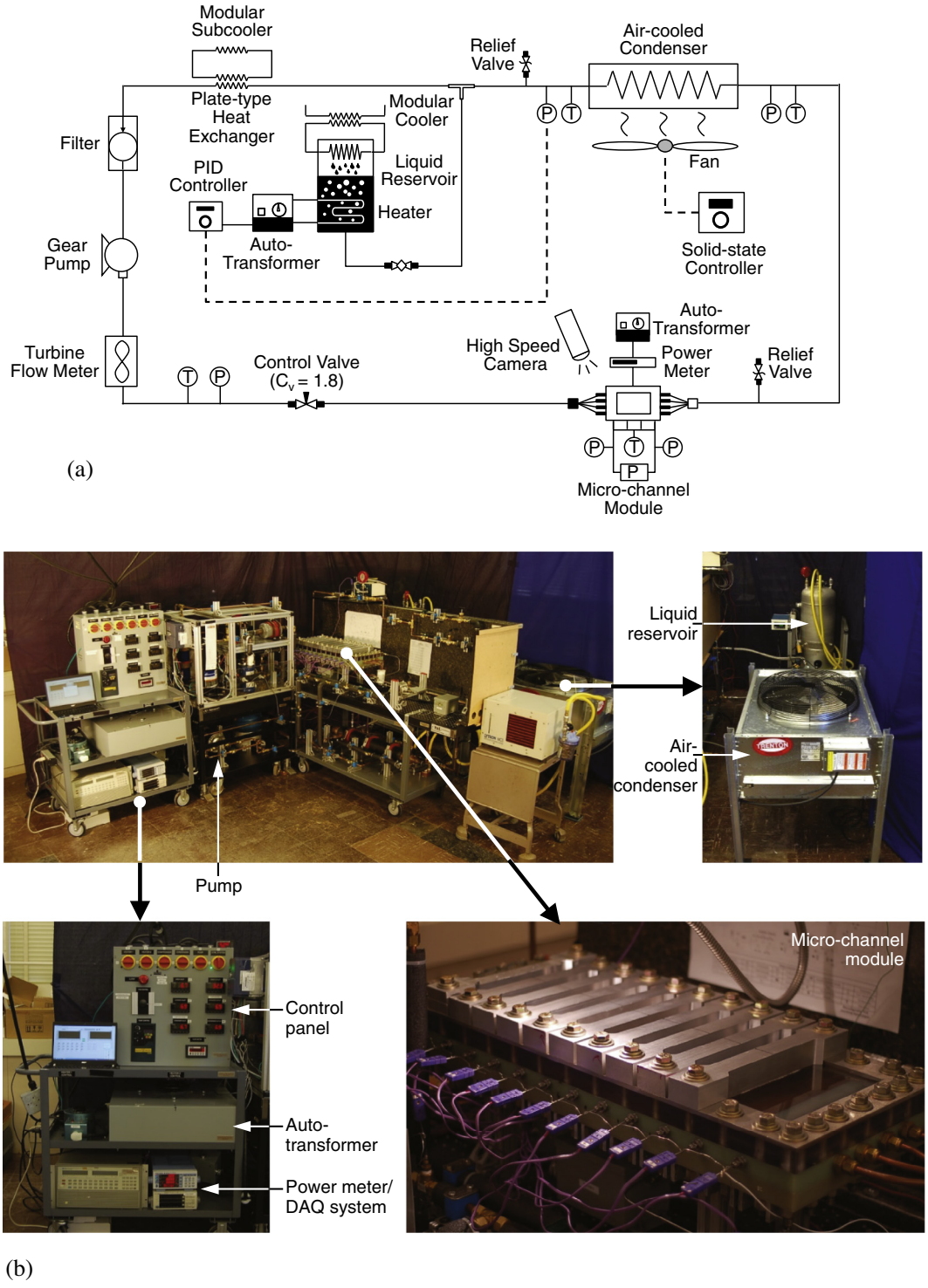

Fig. 2. (a) Schematic diagram of two-phase flow loop. (b) Photos of test facility.

Aside from temperature measurements in the inlet and outlet, temperatures are also measured by a series of type-E thermocouples inserted at 10 axial locations along the centerline of the copper heat sink as indicated in Table 1. The heat sink thermocouples are calibrated over a range from −22.5 to 80 °C in a temperature-controlled thermal bath having a temperature set point accuracy of 0.01 °C. The calibrations are performed against a platinum resistance thermometer having an accuracy of ±0.03 °C. To ensure temperature uniformity, the tips of the thermocouples and thermometer are placed in the bath next to each other and the steady state calibration repeated every 2.5 °C bath temperature increments. Distilled water is used as bath fluid above 7.5 °C and replaced at lower temperatures by 50%-volume ethylene glycol-water mixture to prevent frost formation. Temperature readings of the thermometer and thermocouple are correlated against one another by a least squares scheme using fourth-order polynomial curve fits. Overall, this calibration resulted in a maximum thermocouple error of ±0.1 °C.

Pressure is measured at the inlet and outlet of the microchannel test module by a combination of two Omega-MMA

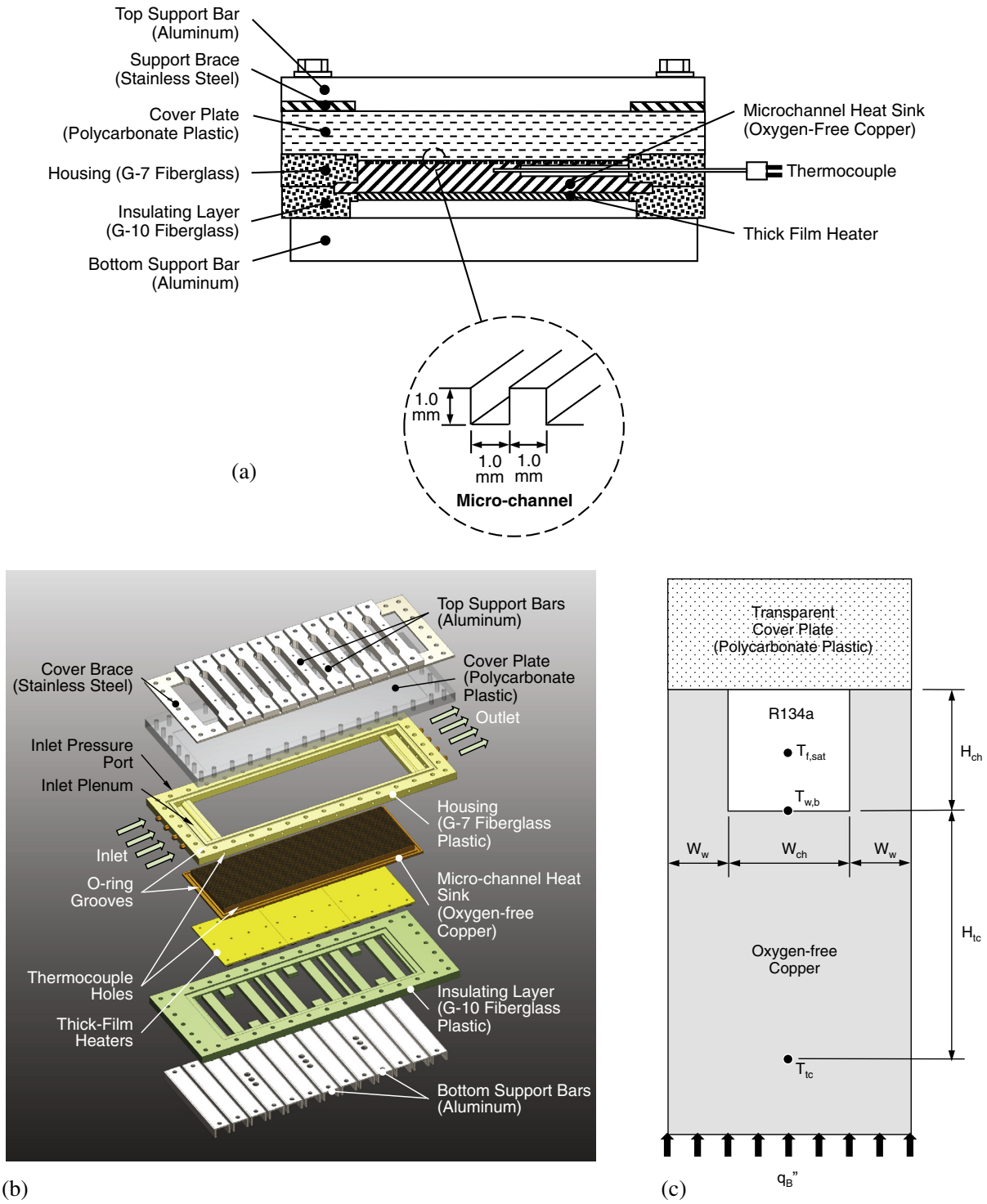

Fig. 3. (a) Cross-sectional view of micro-channel module. (b) Layered layout of module parts. (c) Two-dimensional micro-channel heat sink unit cell.

absolute pressure transducers and a Honeywell-THE differential pressure transducer. Volumetric flow rate is measured by a Flow Technology FTO-series turbine flow meter. A Yokogawa WT310 power meter is used to measure the voltage, current, and power input to the test module's thick-film heaters.

An FET multiplexer is used to collect signals from the thermocouples, pressure transducers, flow meter, and power meter, which are processed by the data acquisition system. Maximum errors in the measurements of absolute pressure, differential pressure, temperature, mass flow rate, and heat input are estimated at ±0.1%, ±0.1%, ±0.1 °C, ±0.12%, and ±0.3%, respectively. Using the root sum square method, the uncertainty propagated in calculation of the heat transfer coefficient, pressure drop, and vapor quality increment are estimated at <13.46%, 0.1%, 0.16%, respectively.

Table 1
Micro-channel heat sink dimensions.

Length [mm]	Width [mm]	Number of channels	Axial locations of thermocouples [mm]
609.6	203.2	100	44.2, 102.1, 160.0, 217.9, 275.8, 333.8, 391.7, 434.3, 507.5, 565.4

2.4. Operating conditions

The test module's inlet quality, $x_{e,in}$, is determined from the relation

$$x_{e,in} = \frac{h_{in} - h_f}{h_{fg}} = -\frac{c_{p,f}(T_{sat} - T_{in})}{h_{fg}}, \quad (2)$$

where $c_{p,f}$, T_{sat}, and h_{fg} are based on saturation pressure measured at the module's inlet, and T_{in} is the measured inlet temperature. The outlet quality is determined by applying an energy balance to the entire module,

$$x_{e,out} = x_{e,in} + (q''_B A_{base})/\dot{m} h_{fg}, \quad (3)$$

where q_B'' is the heat flux based on the 609.6-mm long by 203.2-mm wide surface area, A_{base}, of the heat sink, and $\dot{m}$ the total flow rate of R134a.

Ranges of key parameters of the study are as follows: mass velocity of G = 75.92–208.79 kg/m^2 s, test module's inlet pressure of p_{in} = 688.3–731.3 kPa, heat sink's base heat flux of q_B'' = 3990–28,209 W/m^2, inlet quality of $x_{e,in}$ = −0.041 to −0.022, and outlet quality of $x_{e,out}$ = 0.096–0.956.

2.5. Determination of heat transfer coefficient

Fig. 3(c) shows a unit cell of the heat sink consisting of a single micro-channel and half thicknesses of the copper sidewalls. The two-phase heat transfer coefficient is determined by equating heat input from the underside of the copper heat sink to convection along the channel's bottom and sidewalls, and treating the sidewalls as adiabatic tip fins with fin efficiency η.

$$h = \frac{q''_B(W_{ch} + 2W_w)}{(T_{w,b} - T_{sat})(W_{ch} + 2\,\eta\,H_{ch})}, \quad (4)$$

where $\eta = \tanh(mH_{ch})/(mH_{ch})$ and $m = \sqrt{h/(k_s W_w)}$ [67].

The micro-channel's bottom wall temperature, $T_{w,b}$, in Eq. (4) is calculated by assuming one-dimensional heat conduction between the planes of the thermocouple and micro-channel's bottom wall, $T_{w,b} = T_{tc} - q''_B H_{tc}/k_s$, where H_{tc} and k_s are the distance between the thermocouple junction and micro-channel's bottom wall and thermal conductivity of copper, respectively. The fluid saturation temperature, T_{sat}, in Eq. (4) is based on local saturation pressure calculated by linear interpolation between the test module's inlet and outlet pressures.

3. Experimental results

3.1. Subcooled flow boiling region (x_e < 0)

3.1.1. Transition from partially developed boiling (PDB) to fully developed boiling (FDB)

Bubble nucleation in forced convection is initiated when the wall temperature exceeds the temperature corresponding to the onset of nucleate boiling (ONB), $T_w > T_{w,ONB}$. ONB is initiated from cavities having a particular size corresponding to tangency between two temperature curves, the first corresponding to the temperature 'required' to ensure sufficient superheat, and the second the superheat 'available' in the liquid boundary layer adjacent to the wall [51]. Additional bubbles are generated in the axial direction as the gradual increase in available wall superheat spurs nucleation over a broader spectrum of cavity sizes. The partially developed boiling (PDB) region (also referred to as 'highly subcooled boiling region') is initiated at ONB, and is accompanied by a noticeable drop in wall temperature resulting from an abrupt increase in the heat transfer coefficient. After this localized temperature drop, both the bulk fluid temperature and wall temperature increase gradually until the flow enters the fully developed boiling (FDB) region.

Schematics in Fig. 4(a) and (b) depict bubble behavior in the PDB and FDB regions, respectively. In the PDB region, bubbles are generated only at preferred cavities (corresponding to the tangency criterion) and maintain their size while sliding along the wall. The limited bubble growth is the result of evaporation and condensation at the bubble interface fairly balancing one another in this region. There is also additional single-phase liquid convection occurring along the surface between the sliding bubbles. In the FDB region, Fig. 4(b), more bubbles are generated from a broader range of cavity sizes, resulting in more bubble detachment as well as coalescence. Here, single-phase liquid convection is less consequential, because of both the diminishing surface area available for liquid-wall contact, and heat transfer enhancement resulting from the more vigorous boiling process. This is the reason the upstream edge of the FDB region is the location where the wall temperature is governed by the heat flux relation $q''_H = C\Delta T_{sat}^n = C(T_{w,b} - T_{sat})^n$, similar to pool boiling [55,60,77].

Shown in Fig. 5(a) and (b) for G = 170.83 kg/m^2 s are series of high speed images captured in the PDB region for q_B'' = 8073 W/m^2 s, and FDB region for q_B'' = 12,109 W/m^2 s, respectively. These images were captured using a shutter speed of 0.125 ms (1/8000 s), but only one of every 50 frames (*i.e.*, with a time interval of 6.25 ms) is shown in each series.

In the PDB region, Fig. 5(a), very small bubbles are generated along the bottom walls of the micro-channels, and preserve their size as they slide along because of the strong condensation effects provided by the highly subcooled bulk flow. These small bubbles remain attached to the bottom wall, and are able to detach only when they grow large enough to allow buoyancy to overcome the surface tension force, which is reflected by the relation for bubble detachment diameter $D_b \simeq \sqrt{\sigma/\{g(\rho_f - \rho_g)\}}$ [78,79]. Bubbles

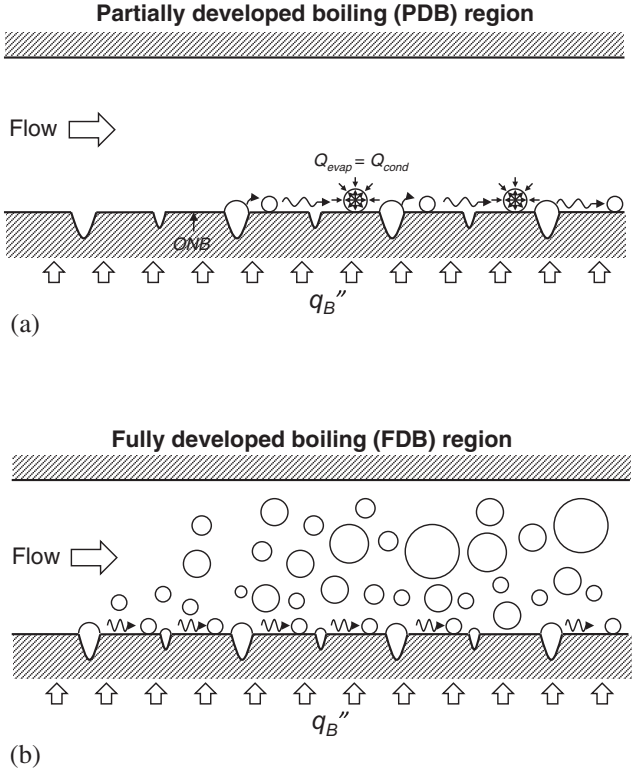

Fig. 4. Schematics of bubble behavior in subcooled boiling: (a) partially developed boiling (PDB) region and (b) fully developed boiling (FDB) region.

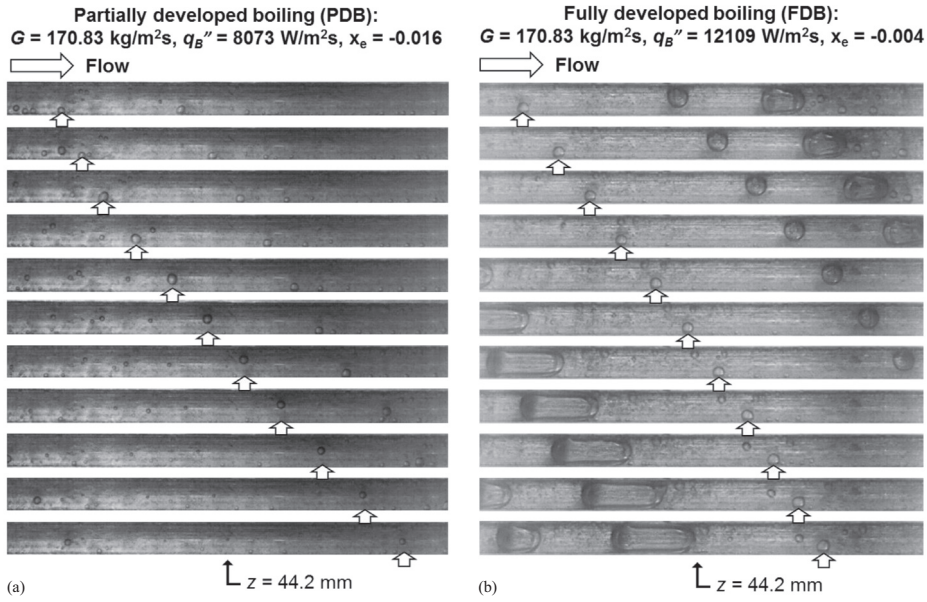

Fig. 5. Flow images centered at $z = 44.2$ mm for $G = 170.83$ kg/m^2 s: (a) partially developed boiling (PDB), and (b) fully developed boiling (FDB). The time interval between individual images in each sequence is 6.25 ms.

generated along the sidewalls appear to remain attached longer because buoyancy is less effective at causing detachment along these walls. However, larger bubbles are formed along the sidewalls by coalescence of nearby smaller bubbles, and these larger bubbles sometimes engulf smaller bubbles still attached to the bottom wall. The newly formed larger bubbles are then sheared off the heated walls and brought into the highly subcooled liquid bulk flow, where they get smaller because of the strong condensation effects.

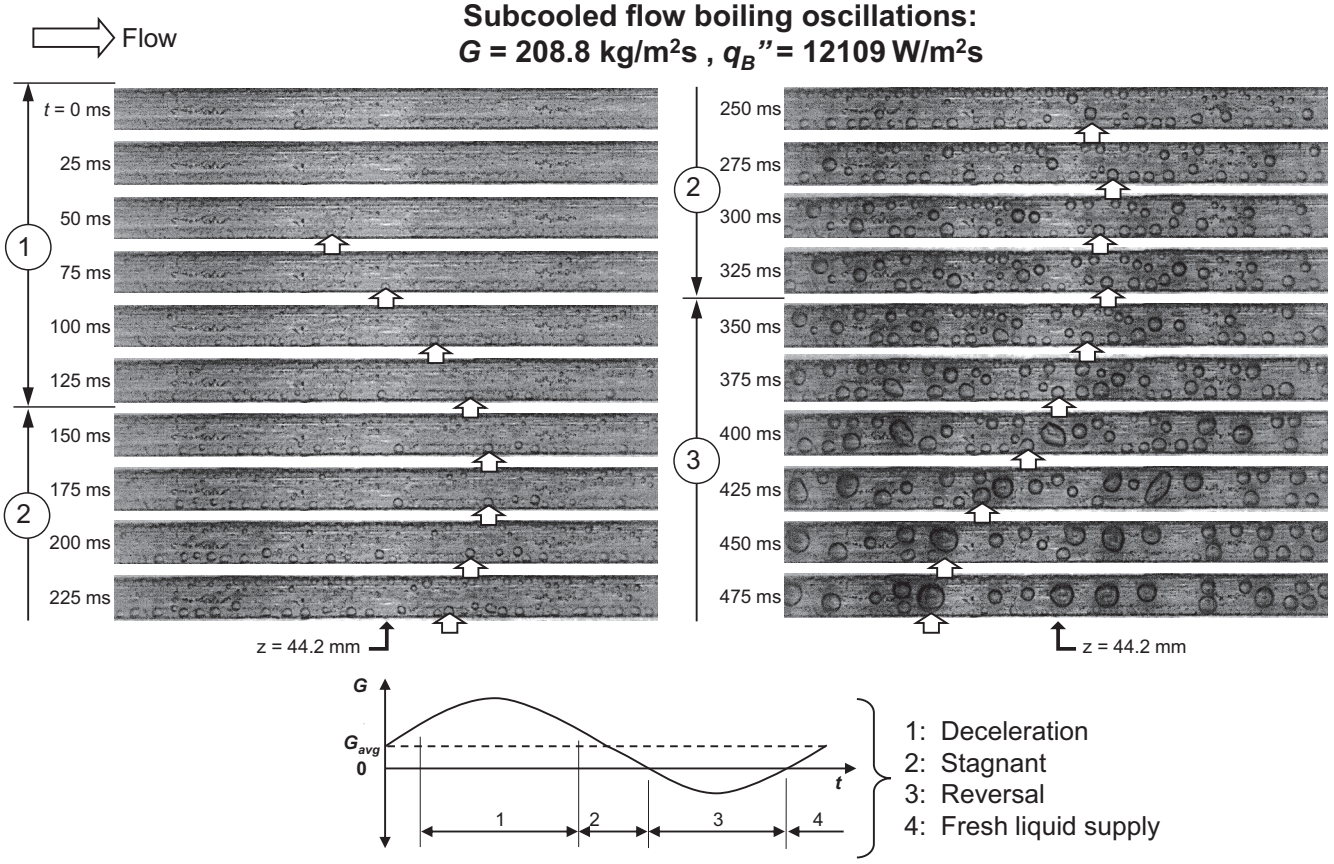

Fig. 6. Images centered at $z = 44.2$ mm capturing subcooled flow boiling oscillations for $G = 208.8$ kg/m^2 s and $q_B'' = 12{,}109$ W/m^2 s.

Both the wall and bulk fluid temperatures increase as the heat flux is increased from q_B'' = 8073 W/m^2, Fig. 5(a), to 12,109 W/m^2, Fig. 5(b). At the higher flux, which corresponds to FDB, relatively weak bulk liquid subcooling allows more bubbles to nucleate along the bottom wall. Bubbles can also more easily grow and coalesce with one another to form larger bubbles that are able to detach from the bottom wall. As shown in Fig. 5(b), bubbles that are generated along the sidewalls slide along the sidewalls but grow bigger by coalescing with smaller bubbles before detaching by liquid shear or merging into much larger bubbles. Notice that the oblong bubbles filling the entire cross-sectional area, which are captured in the last seven frames in Fig. 5(b), are mostly the result of instabilities causing the vapor to flow backwards to the inlet plenum before flowing again along the flow direction. As discussed in [14], the vapor backflow is a cause for intermittent dryout and CHF in the downstream region of the channel. These issues will be discussed in more detail later in this paper.

It should be emphasized that the transition between PDB and FDB in the subcooled boiling region does not occur systematically at a particular axial location for a given set of operating conditions. In fact, there is overlap between PDB and FDB that results mostly from periodic flow oscillations. This overlap is captured in a sequence of images in Fig. 6 corresponding to z = 44.2 mm, G = 208.8 kg/m^2 s, and q_B'' = 12,109 W/m^2 s; individual images are separated by 25 ms. A qualitative plot of instantaneous mass velocity is provided to help explain the role of instabilities in subcooled boiling. The period of oscillation is initiated at the peak G value during period 1, from 0 to 125 ms. Here, very small bubbles, barely visible to the naked eye, move downstream and just begin to grow by coalescing with sidewall bubbles, phenomena that are representative of mostly PDB. Increased flow resistance associated with the bubble formation causes a decline in mass velocity and therefore pressure drop. In period 2, from 150 to 325 ms, the mass velocity momentarily drops to near zero, allowing for abundant nucleation to take effect, which represents a transition from PDB to FDB. In period 3, from 350 to 475 ms, bubbles formed during period 2 undergo appreciable coalescence, evidenced by a large increase in void fraction, which greatly increases flow resistance, causing a reversal in the flow direction. As the backflow purges the vapor from the upstream region of the channel, low flow resistance fresh liquid entering the channel gradually increases mass velocity before decreasing again within period 1 of a new oscillation cycle. These flow oscillations suggest some overlap between PDB and FDB in the subcooled boiling region that are also influenced by the vapor backflow. Associated with the transition from PDB to FDB are significant variations of void fraction along the channel.

Shah [61] employed the following dimensionless parameters to correlate the transition from PDB to FDB:

$$\frac{\psi}{\psi_0} = \frac{q_H''/[h_{sp}(T_{w,b} - T_{sat})]}{\psi_0}, \tag{5}$$

$$\frac{\Delta T_{sub}}{\Delta T_{sat}} = \frac{T_{sat} - T_f}{T_{w,b} - T_{sat}}, \tag{6}$$

and

$$Bo = \frac{q_H''}{G h_{fg}}, \tag{7}$$

where ψ is the ratio of average wall heat flux to single-phase heat flux based on heated wall surface area, ψ_0 is the value of ψ corresponding to x_e = 0, $\Delta T_{sub}/\Delta T_{sat}$ is the ratio of subcooling to wall superheat, and Bo is the boiling number. Shah recommended the following dependence of ψ_0 on the boiling number, Bo:

$$\psi_0 = 230\,Bo^{0.5} \quad \text{for } Bo > 0.3 \times 10^{-4} \tag{8a}$$

and

$$\psi_0 = 1 + 46\,Bo^{0.5} \quad \text{for } Bo < 0.3 \times 10^{-4}. \tag{8b}$$

Notice that the definitions of individual parameters in Eqs. (5)–(8b) are adjusted to reflect the specific geometry of the present study. Specifically, q_H'' in Eqs. (5) and (7) is the heat input averaged over the three heated channel walls, and $T_{w,b}$ in Eqs. (5) and (6) is the measured bottom wall temperature of the micro-channel. Also, T_f in Eq. (6) is the bulk fluid temperature at axial location z calculated according to

$$T_f = T_{in} + \frac{q_B''(W_{ch} + 2W_w)}{G(W_{ch}H_{ch})c_{p,f}} z. \tag{9}$$

where T_{in} is the measured inlet plenum temperature.

Fig. 7(a) shows the variation of ψ/ψ_0 with $\Delta T_{sub}/\Delta T_{sat}$ for the present data. Notice how data for PDB and FDB are clearly segregated around $\Delta T_{sub}/\Delta T_{sat}$ = 2. Superimposed in the same figure are Shah's predictions for PDB and FDB, as well as the transition between the two regions, which are given by [61]

$$FDB: \quad \frac{\psi}{\psi_0} = 1 \quad for \ \frac{\Delta T_{sub}}{\Delta T_{sat}} < 2 \tag{10a}$$

and

$$PDB: \quad \frac{\psi}{\psi_0} = 0.54\left(\frac{\Delta T_{sub}}{\Delta T_{sat}}\right)^{0.88} \quad for \ \frac{\Delta T_{sub}}{\Delta T_{sat}} > 2. \tag{10b}$$

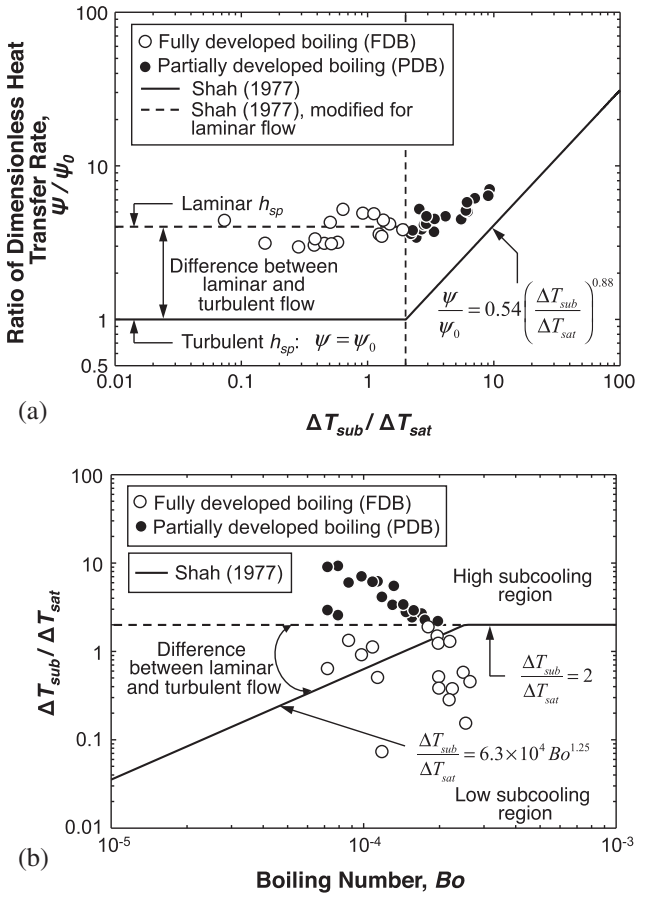

Fig. 7. Transition between partially developed boiling (PDB) and fully developed boiling (FDB) regions compared to Shah's [61] predictions: (a) ratio of dimensionless heat transfer rate, ψ/ψ_0, versus $\Delta T_{sub}/\Delta T_{sat}$, and (b) $\Delta T_{sub}/\Delta T_{sat}$ versus boiling number, Bo.

Table 2
Dimensionless subcooled boiling and single-phase correlations.

Author(s)	Correlation	MAE (%)	Remarks
Papell [83]	$\frac{Nu_{sc}}{Nu_{sp}} = 90\left(\frac{q''_H}{h_{fg}\rho_g V_b}\right)^{0.7}\left(\frac{h_{fg}}{c_{pf}\Delta T_{sub}}\right)^{0.84}\left(\frac{\rho_g}{\rho_f}\right)^{0.756} = 90\,Bo^{0.7}Ja^{*-0.84}(\rho_g/\rho_f)^{0.056}$ $Nu_{sp} = 0.021Re_f^{0.8}\,Pr_f^{0.4}$	131.03	– Single-phase heat transfer coefficient in Nu_{sp} based on Colburn type correlation for turbulent flow [84] – Based on data for distilled water as well as liquid ammonia data from another source – Inconel X tube – FDB data only
Modified Papell [83]	$\frac{Nu_{sc}}{Nu_{sp}} = 90\left(\frac{q''_H}{h_{fg}\rho_g V_b}\right)^{0.7}\left(\frac{h_{fg}}{c_{pf}\Delta T_{sub}}\right)^{0.84}\left(\frac{\rho_g}{\rho_f}\right)^{0.756} = 90\,Bo^{0.7}Ja^{*-0.84}(\rho_g/\rho_f)^{0.056}$	80.93	– Single-phase heat transfer coefficient in Nu_{sp} based on correlation for laminar flow in a rectangular channel with three-sided heating by Shah and London [82] – Based on data for distilled water as well as liquid ammonia data from another source – Inconel X tube – FDB data only
Badiuzzaman [85]	$\frac{Nu_{sc}}{Nu_{sp}} = C\left\{\left(\frac{q''_H}{h_{fg}\rho_g V_b}\right)\left(\frac{h_{fg}}{c_{pf}\Delta T_{sub}}\right)^{1.2}\left(\frac{\rho_g}{\rho_f}\right)^{1.08}\left(\frac{\Delta T_{sub}}{T_{sat}}\right)^{0.6}\right\}^m = C\left\{Bo\,Ja^{*-1.2}(\rho_g/\rho_f)^{0.08}(\Delta T_{sub}/T_{sat})^{0.6}\right\}^m$ Water: $C = 178$, $m = 0.75$ Organic fluids: $C = 759$, $m = 0.89$	25.67	– Single-phase heat transfer coefficient in Nu_{sp} based on correlation for laminar flow in a rectangular channel with three-sided heating by Shah and London [82] – Based on data for water, ethyl alcohol, and isopropyl alcohol – Stainless steel 321 tube – FDB data only
Moles and Shaw [86]	$\frac{Nu_{sc}}{Nu_{sp}} = \left(\frac{q''_H}{h_{fg}\rho_g V_b}\right)^{0.67}\left(\frac{h_{fg}}{c_{pf}\Delta T_{sub}}\right)^{0.5}\left(\frac{\rho_g}{\rho_f}\right)^{0.7}\left(\frac{c_{pf}\mu_f}{k_f}\right)^{0.46} = 78.5\,Bo^{0.67}Ja^{*-0.5}(\rho_g/\rho_f)^{0.03}Pr_f^{0.46}$	19.37	– Single-phase heat transfer coefficient in Nu_{sp} based on correlation for laminar flow in a rectangular channel with three-sided heating by Shah and London [82] – Based on data for water, ethyl alcohol, isopropyl alcohol, N-butyl alcohol, ammonia, aniline, and hydrazine from ten different sources – Stainless steel 347, 304, and 321, Inconel, Inconel X, and nickel L – Variety of channel geometries – FDB data only
Shah and London [82]	$Nu_{sc} = (Nu_{devel}^4 + Nu_3^4)^{1/4}$ $Nu_{devel} = 1.54\left(\frac{L_{sp}}{Re_f\,Pr_f D_h}\right)^{-0.33}$ $Nu_3 = 8.235\,(1 - 1.833\beta + 3.767\beta^2 - 5.814\beta^3 + 5.361\beta^4 - 2.0\beta^5)$	69.27	– Single-phase laminar flow in a rectangular channel with three-sided heating [82]

Fig. 7(a) shows Shah's original correlations underpredict the data for both the PDB and FDB regions. It should be noted that Shah's original correlations are based on the assumption of turbulent single-phase flow, where [61,80,81]

$$\frac{h_{sp}\,D_h}{k_f} = Nu_{turb} = 0.023Re_{sp}^{0.8}\,Pr_f^{0.4}, \tag{11}$$

whereas the highest liquid Reynolds number in the present study is $Re_f = 1120.2$, well within the laminar range; laminar liquid flow is also prevalent in most micro-channel flows. To correct for the turbulent flow assumption, a dashed line corresponding to Shah's predictions modified for laminar single-phase flow is also included in Fig. 7(a) for the FDB region. The single-phase heat transfer coefficient, h_{sp}, corresponding to the dashed line is calculated as follows [82]:

$$\frac{h_{sp}\,D_h}{k_f} = Nu_{lam} = (Nu_{devel}^4 + Nu_3^4)^{1/4}, \tag{12}$$

where

$$Nu_{devel} = 1.54\left(\frac{L_{sp}}{Re_f\,Pr_f D_h}\right)^{-0.33} \tag{13a}$$

and

$$Nu_3 = 8.235(1 - 1.833\beta + 3.767\beta^2 - 5.814\beta^3 + 5.361\beta^4 - 2.0\beta^5). \tag{13b}$$

In Eqs. (12) and (13b), Nu_3 is the Nusselt number for 3-sided heated rectangular channels, and β is the channel cross-section's aspect ratio ($\beta < 1$). Notice in Fig. 7(a) that the laminar flow assumption yields higher values for ψ/ψ_0. The constant offset between the turbulent and laminar assumptions stems from the smaller ratio of single-phase to total heat transfer rate achieved in micro-channels compared to macro-channels. Overall, Fig. 7(a) shows that, despite deviations between Shah's predictions and the present data, his relation $\Delta T_{sub}/\Delta T_{sat} = 2$ accurately predicts the transition from PDB to FDB, regardless of the assumptions used to calculate h_{sp}. PDB and FDB data are further segregated by plotting $\Delta T_{sub}/\Delta T_{sat}$ versus Bo, Fig. 7(b). The Shah relations are expressed as [61]

$$\frac{\Delta T_{sub}}{\Delta T_{sat}} = 6.3\times 10^4 Bo^{1.25} \text{ for } \frac{\Delta T_{sub}}{\Delta T_{sat}} < 2. \tag{14a}$$

and

$$\frac{\Delta T_{sub}}{\Delta T_{sat}} = 2 \text{ for } \frac{\Delta T_{sub}}{\Delta T_{sat}} \geqslant 2. \tag{14b}$$

For equal Bo values, Fig. 7(b) shows the predicted transition from FDB to PDB occurs at a higher value of $\Delta T_{sub}/\Delta T_{sat}$ for laminar compared to turbulent h_{sp}. Here too, there are appreciable deviations in the Shah predictions when using laminar instead of turbulent relations for h_{sp}. The inability to predict the present data points to the need for further investigation of the transition from PDB to FDB in micro-channels.

3.1.2. Assessment of previous heat transfer coefficient correlations for subcooled flow boiling

Five dimensionless correlations listed in Table 2 are assessed for accuracy in predicting the subcooled boiling heat transfer coefficient; results are shown in Fig. 8(a)–(e). In this assessment, the thermophysical properties of R134a are acquired from NIST's REFPROP 8.0 [87]. The accuracy for each correlation is evaluated using three different parameters: MAE, θ, and ξ. The former is mean absolute error, which is defined as

$$MAE(\%) = \frac{1}{N}\sum\left[\frac{|h_{pred} - h_{exp}|}{h_{exp}} \times 100\right], \tag{15}$$

while θ and ξ are the percentages of data points predicted within ±30% and ±50%, respectively. As recommended in [67], correlations intended for circumferentially uniformly heated channels (circular or rectangular with four-sided heating) are modified by relation

$$h_{pred} = h_{cor}\frac{Nu_3}{Nu_4} \tag{16}$$

where h_{cor} corresponds to the value predicted by the original correlation. In Eq. (16), Nu_4 is the Nusselt number for thermally developing laminar flow with four-sided heating, which is given by [82],

$$Nu_4 = 8.235(1 - 2.042\beta + 3.085\beta^2 - 2.477\beta^3 + 1.058\beta^4 - 0.186\beta^5). \tag{17}$$

Notice in Fig. 8(a)–(e) that the individual correlations tested are compared to all present subcooled boiling data, which include PDB and FDB data, segregated using solid and open symbols, respec-

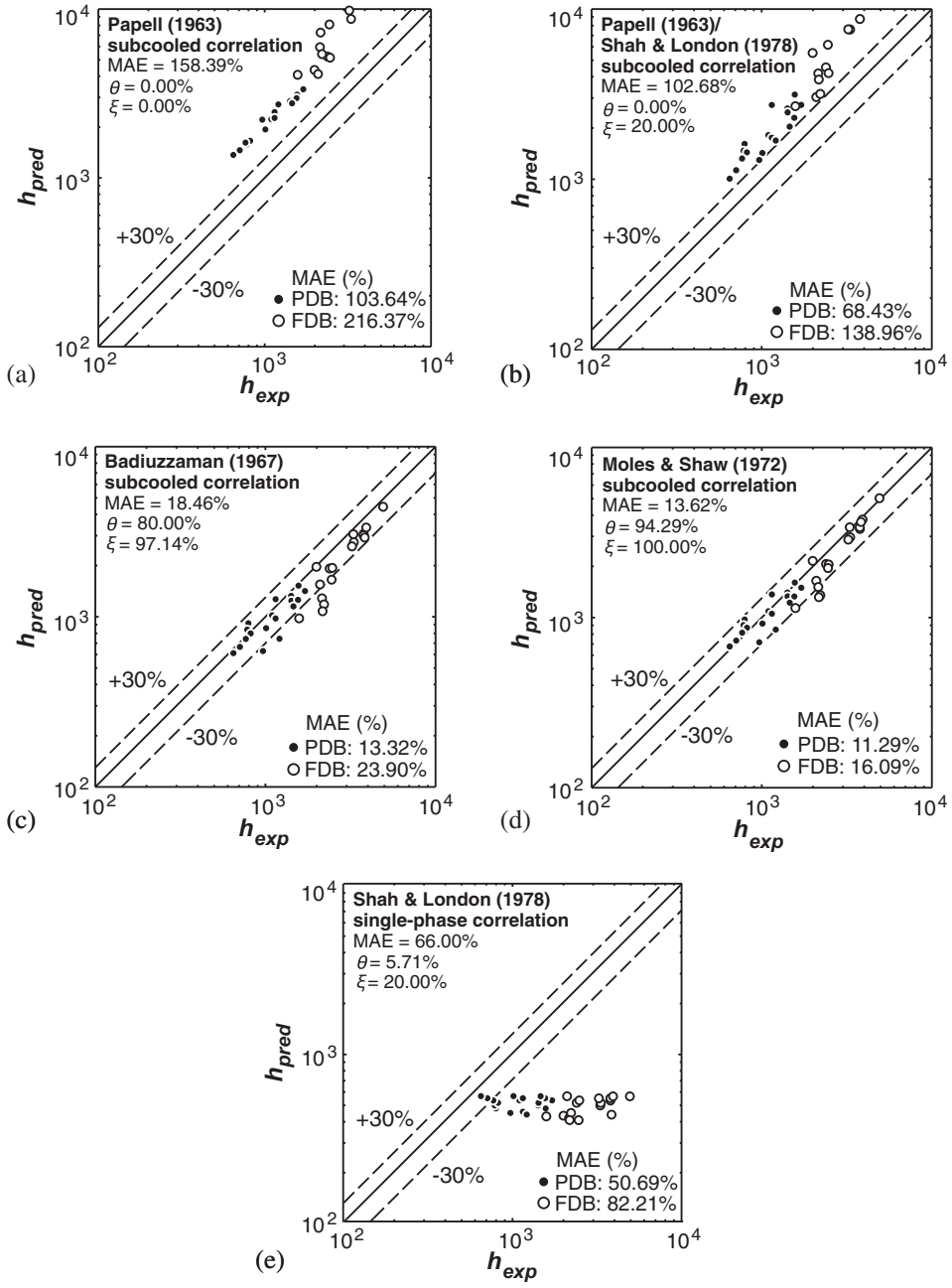

Fig. 8. Comparison of present subcooled heat transfer coefficient data with predictions of empirical subcooled correlations of: (a) Papell [83], (b) Papell [83]/Shah and London [82], (c) Badiuzzaman [85], and (d) Moles and Shaw [86], and single-phase correlation of (e) Shah and London [82].

tively. Table 2 shows that these correlations are presented as Nu_{sc}/Nu_{sp}, the ratio of the subcooled two-phase Nusselt number to the single-phase Nusselt number. This is also equal to h_{sc}/h_{sp}, the ratio of the subcooled boiling heat transfer coefficient to the single–phase heat transfer coefficient. It should be noted that Papell's original correlation [83] employs a turbulent Colburn type single-phase correlation [84] in which the coefficient in the original Colburn correlation was replaced with a different value (0.021) to achieve better agreement with Papell's single-phase heat transfer data. The single-phase convection heat transfer coefficient in all the other correlations is based on Shah and London's relation for laminar flow in a rectangular channel with three-sided heating, Eq. (12).

Overall, Fig. 8(a)–(e) show that all the correlations tested yield far better accuracy in predicting PDB versus FDB data. As shown in Fig. 8(a), Papell's correlation, which is based on a modified turbulent Colburn single-phase correlation, shows relatively poor accuracy. By replacing the modified Colburn correlation by Shah and London's laminar single-phase correlation as described above, the accuracy of the Papell correlation is improved somewhat as shown in Fig. 8(b), with the MAE for all PDB and FDB data combined decreasing from 158.39% to 102.68%. This is consistent with the earlier discussion in conjunction with Fig. 7(a) concerning improved prediction of ψ when using the laminar flow assumption. Limited accuracy of the Papell's correlation can be attributed to its reliance on data for water and ammonia, which both possess thermophysical properties significantly superior to those of R134a. Fig. 8(c) shows far better predictions are achieved with the correlation by Badiuzzaman [85], evidenced by a MAE of only 18.46%. While originally developed for only FDB data for water and two different alcohols, Fig. 8(c) shows the same correlation is quite effective in predicting PDB data as well. With a MAE of only 13.62%, the most successful of all correlations tested is the one by Moles and Shaw [86], Fig. 8(d), which is based on FDB data for ten different fluids from multiple sources. Interestingly, both the Badiuzzaman and Moles and Shaw correlations capture a noticeable discontinuity in predicting PDB versus FDB data.

For reference, predictions based entirely on Shah and London's [82] single-phase correlation for laminar flow in a rectangular channel (*i.e.,* by replacing h_{sc} by h_{sp}) are also provided. Fig. 8(e) shows that, despite the subcooled flow conditions, this approach yields unusually large errors because of its failure to account for bubble nucleation effects.

To further investigate the predictive capabilities of the different correlations, two-phase heat transfer coefficient and bottom wall temperature predictions are compared to the present data in Fig. 9(a) and (b), respectively, for $G = 212.29$ kg/m^2 s, $q_B'' = 4039$ W/m^2, and $x_{e,in} = -0.038$. Fig. 9(a) shows the measured heat transfer coefficient increases appreciably when transitioning from PDB to FDB. Both the Badiuzzman and the Moles and Shaw correlations capture the variation of the heat transfer coefficient in the subcooled region quite well. On the other hand, both the original and modified Papell correlations greatly overpredict the data. Notice also that Shah and London's single-phase correlation both underpredicts the data and follows a trend opposite to that of the data. For reference, Fig. 9(b) shows several important predicted temperature trends, including the linear rise in equilibrium fluid temperature, T_f, until it reaches the saturation temperature, T_{sat}, at $x_e = 0$, following which $T_f = T_{sat}$. These 'equilibrium' calculations assume the vapor generation is initiated at the location where $x_e = 0$ and therefore ignore the subcooled boiling effects altogether. Also included in Fig. 9(b) is the wall temperature corresponding to ONB, which is predicted according to Sato and Matsumura's model [53]. Fig. 9(b) also shows PDB occurring at $z = 44.2$ and 102.1 mm, followed by FDB at $z = 160.0$ mm, all

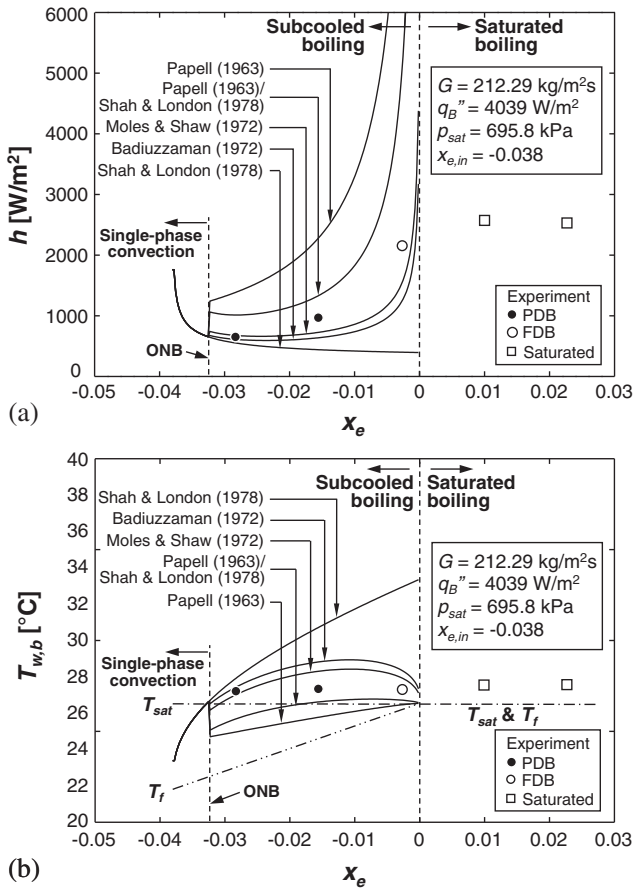

Fig. 9. Subcooled boiling regime development along the micro-channels: (a) local heat transfer coefficient, and (b) local bottom wall temperature compared with predictions of subcooled boiling correlations. Data shown are measured at $z = 44.2$, 102.1, 160.0, 217.9, and 275.8 mm.

downstream from ONB. Here too, both the Badiuzzman and the Moles and Shaw correlations show fairly good predictions of the wall temperature data.

3.2. Saturated flow boiling region ($x_e > 0$)

3.2.1. Flow oscillations

Periodic flow oscillations are commonly encountered in two-phase micro-channels because bubbles grow rapidly to occupy the entire cross-section. These instabilities are manifest in periodic oscillations in mass velocity, which are responsible for pressure oscillations between the inlet and outlet plenums. Fig. 10 shows a series of schematics of *transient* flow patterns observed in the present study based on extensive analysis of video records. From a temporal standpoint, a single oscillation period consists of six sub-periods. Notice that the micro-channel is divided spatially into four distinct sections; flow within each varies during the successive sub-periods.

Sub-period t_1 corresponds to initiation of the instability period, where increased pressure in the inlet plenum causes a substantial increase in mass velocity, causing a surge of liquid into the channel, which results in peak value for mass velocity between t_1 and t_2. During t_1, the upstream plenum contains a vapor/liquid mixture, but the relatively high mass velocity associated with onset of the surge tends to suppress bubble nucleation in section 1. During the same sub-period, the downstream sections still suffer significant liquid deficiency from the previous instability period, and are dominated by annular liquid film evaporation. A thin annular liquid film is maintained in sections 2 and 3, while section 4 under-

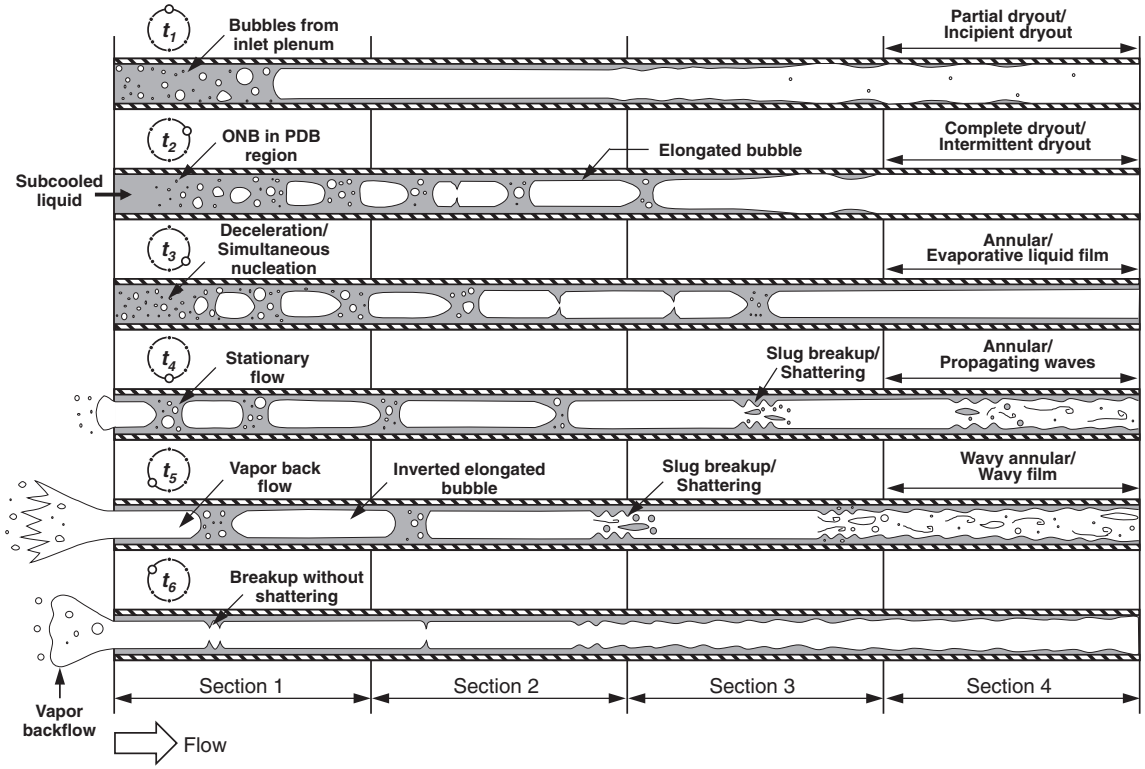

Fig. 10. Schematic renderings of transient flow patterns observed at six different times within a single periodic cycle: t_1: beginning of the cycle, t_2: forward liquid advance, t_3: rapid bubble growth, t_4: commencement of transition pattern, t_5: commencement of wavy annular pattern, and t_6: end of liquid deficient period. The indicated sections are as follows: 1: subcooled boiling dominant, 2: combined saturated nucleate and convective boiling, 3: saturated convective boiling by annular film evaporation, and 4: intermittent dryout dominant region.

goes partial liquid film dryout (also known as incipient dryout), where heat transfer is compromised.

Sub-period t_2 is dominated by forward advance of liquid from upstream with a slight decrease in mass velocity from peak value, while still large enough to suppress bubble nucleation upstream. In section 1, the flow enters the channel in mostly subcooled liquid state, resulting in single-phase liquid convection near the inlet, followed by subcooled flow boiling. Section 2 is occupied mostly by slug flow resulting from bubble coalesce. Section 3 now includes remnants of the annular film from t_1, which undergoes temporary dryout (also termed intermittent dryout) in section 4, causing significant reduction in the heat transfer coefficient.

Sub-period t_3 is dominated by rapid bubble growth and coalescence into oblong bubbles, causing flow acceleration downstream and a slowdown upstream. Absent in section 1 is upstream pure liquid flow, and the upstream slowdown triggers appreciable bubble nucleation and growth in the same section. Section 2 is now dominated by slug flow, and section 3 by combined slug and annular flow. Downstream, section 4 begins to take advantage of the liquid surge from the prior sub-periods, with an annular liquid film being gradually established and heat transfer dominated by liquid film evaporation.

Sub-period t_4 corresponds to a transitional time when increased void fraction from sub-period t_3 greatly increases flow resistance, resulting in appreciable flow slowdown and a halt to incoming flow, which is followed by vapor backflow into the inlet plenum. The slowdown spurs appreciable bubble nucleation and coalescence into large oblong bubbles in section 1. The large increase in vapor production reduces the length of liquid slugs in section 2, and causes a shattering of the liquid slugs into droplets in section 3 that are entrained into section 4. The downstream end of section 4 begins to incur wavy annular flow, with an abundance of the shattered liquid drops in the core.

During sub-period t_5, the vapor backflow into the inlet plenum becomes very pronounced and bubble shape is inverted in section 1 because of the flow reversal. Farther downstream, wavy annular flow is established in the downstream end of section 3 and throughout section 4.

Sub-period t_6 marks a duration of liquid deficiency, where bubbles cast earlier into the inlet plenum mix with the plenum's subcooled liquid, increasing the inlet liquid temperature. Sections 1 and 2 show liquid slug breakups without droplet shattering, and relatively mild evaporation. With the liquid deficiency, the intensity of propagating waves in sections 3 and 4 is subdued. The inlet plenum pressure now reaches peak value, pushing the flow through the channel once more and initiating a new instability period. This also marks the beginning of the increase in mass velocity due to liquid surge at the channel inlet, while liquid deficiency is maintained in the rest of the micro-channel.

Fig. 11(a) and (b) depict sequences of high-speed video images capturing flow reversal in the bubbly/slug regime flow, and liquid slug breakup and droplet shattering, respectively. The complex interfacial behavior captured in these figures clearly points to a need for comprehensive and user-friendly *transient* flow regime maps for two-phase micro-channel flow.

3.2.2. Transient flow regime maps

Tables 3 provides a summary of selected previous investigations of flow regime maps for adiabatic, boiling, and condensing flows in micro-channels and macro-channels. This is followed in Table 4 by a list of parameters often adopted in flow regime maps. Overall, the maps can be grouped into two main categories: those that are based on force balance and the others on phase change. Recently, studies have shown that, for both flow boiling and flow condensation, two-phase regimes in micro-channels can be effectively demarcated using the following relations for modified Weber

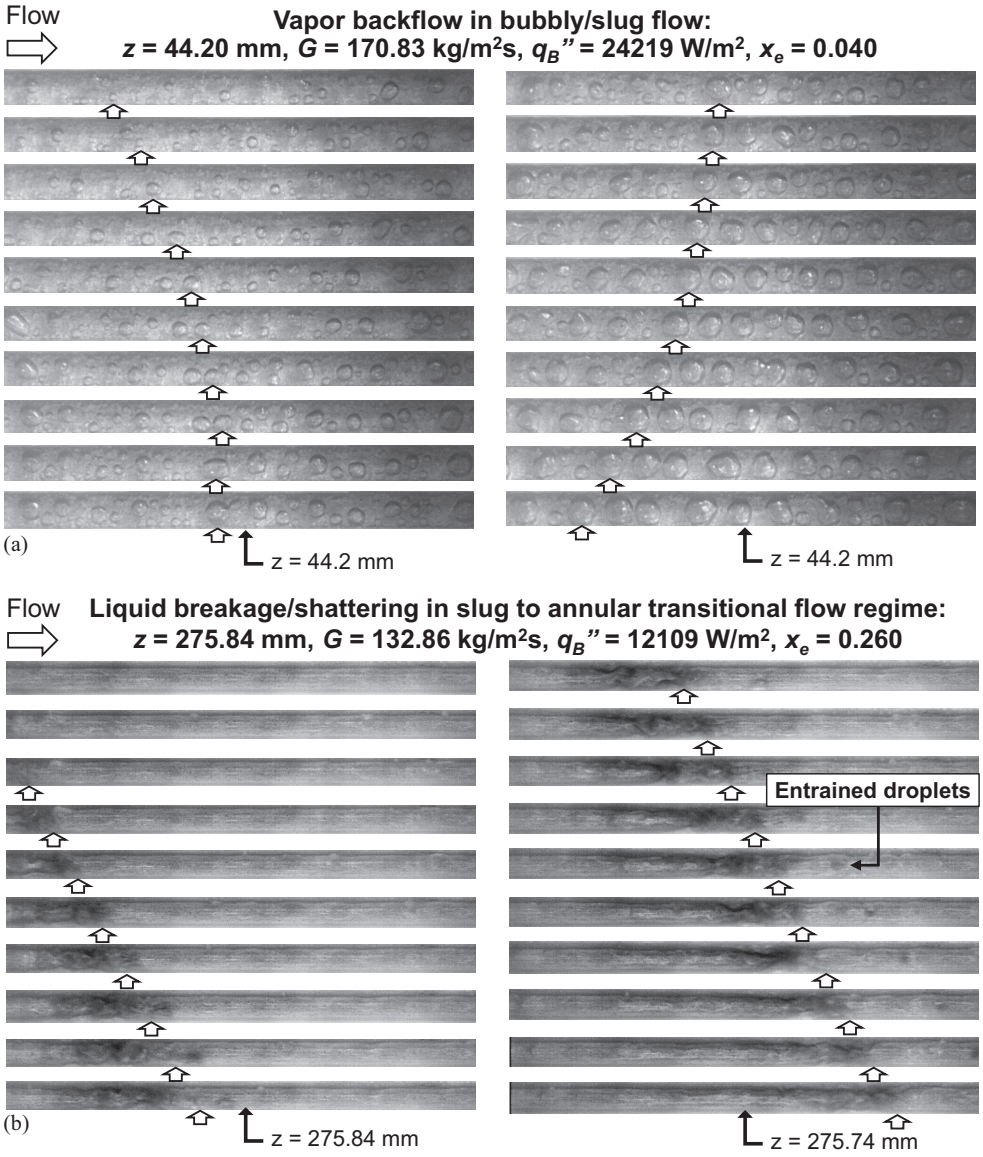

Fig. 11. High speed video images capturing (a) vapor backflow in the bubbly/slug flow, and (b) liquid slug breakup and droplet shattering in the slug to annular transition flow regime. The time interval between consecutive images is 6.25 ms.

number, We^*, as a function of the turbulent-turbulent Lockhart-Martinelli parameter, X_{tt} [65,97]:

$$We^* = 2.45\frac{Re_g^{0.64}}{Su_g^{0.3}(1+1.09X_{tt}^{0.039})^{0.4}} \quad for\ Re_f \leqslant 1250 \tag{18a}$$

and

$$We^* = 0.85\frac{Re_g^{0.79}X_{tt}^{0.157}}{Su_g^{0.3}(1+1.09X_{tt}^{0.039})^{0.4}}\left[\left(\frac{\mu_g}{\mu_f}\right)^2\left(\frac{v_g}{v_f}\right)\right]^{0.084} \quad for\ Re_f > 1250, \tag{18b}$$

where $Re_f = (1-x)GD_h/\mu_f$ and the definitions for Re_g, X_{tt}, and Su_g are provided in Table 4.

As discussed earlier, transient flow regimes encountered in this study are comprised of bubbly/slug, slug, transition, and annular flow regimes, the latter with two dryout sub-categories. Using the present flow regime database of 200 points, new correlations are developed for transitional boundaries between regimes. Fig. 12(a) shows the present data demarcated at $Re_g = 2000$, corresponding to transition from laminar to turbulent vapor flow, to assess the effects of vapor core shear stress on flow regime transitions. Notice that values above and below $Re_g = 2000$ are clearly segregated by a horizontal line corresponding to $We^* = 3$.

Using the new data, a new transient flow regime map is proposed. Fig. 12(b) shows clear segregation between flow regimes around three boundary lines:

$$\text{bubbly/slug to slug}: We^* = 0.95X_{tt}^{0.67}, \tag{19a}$$

$$\text{slug to transition}: We^* = 4.8X_{tt}^{0.48}, \tag{19b}$$

and

$$\text{transition to annular}: We^* = 13.5X_{tt}^{0.38}, \tag{19c}$$

where We^* is defined in Eqs. (18a) and (18b). Interestingly, the transition regime commences above $We^* = 3$, the boundary between laminar and turbulent vapor flow, as shown in Fig. 12(a), and below $X_{tt} = 1$, which suggests the following boundaries for this regime:

$$\text{Transition regime}: We^* \geqslant 3 \text{ and } X_{tt} \leqslant 1. \tag{20}$$

Table 3
Details of prior flow regime maps.

Author(s)	Coordinate parameters	Channel type	Fluid(s)	Remarks
Flow boiling regime maps				
Hetsroni et al. [88]	Re_f vs q^* $Re_f = \frac{j_f D_h}{\nu_f}$ $q^* = \left(\frac{q''_B}{G c_p \Delta T}\right)\left(\frac{T_{w,max}}{T_{w,avg}}\right)$	– Parallel micro-channel heat sink – Horizontal flow	Air-water, steam-water	Triangular: D_h = 0.103–0.161 mm Dryout regimes
Wojtan et al. [89]	G vs x	– Single macro-channel tube – Horizontal flow	R22, R410A	Circular: D_h = 13.84 mm Dryout regimes
Revellin and Thome [50]	G vs x	– Single micro-channel tube – Horizontal flow	R134a, R245fa	Circular: D_h = 0.509, 0.790 mm
Wang and Bergles [90]	q_H'' vs G, q_H'' vs x_e	– Parallel micro-channel heat sink – Horizontal flow	Water	Trapezoidal: D_h = 0.186 mm (427 × 208 × 146 μm)
Adiabatic flow regime maps				
Triplett et al. [91]	j_f vs j_g	– Single micro-channel tube – Horizontal flow	Air-water	Circular: D_h = 1.1, 1.45 mm Semi-triangular: D_h = 1.09, 1.49 mm
Kawahara et al. [92]	j_f vs j_g	– Single micro-channel tube – Horizontal flow	N_2-water	Circular: D_h = 100 μm
Qu et al. [93]	j_f vs j_g	– Parallel micro-channel heat sink – Horizontal flow	N_2-water	Rectangular: W_{ch} = 231 μm H_{ch} = 712 μm
Hassan et al. [94]	j_f vs j_g	– Single micro-channel tube – Horizontal/vertical flow	Air-water	Circular: D_h = 1.0, 0.8 mm
Unstable flow boiling regime maps				
Saha et al. [95]	N_{sub} vs N_{pch}	– Single macro-channel tube – Vertical flow	Freon-113	Circular: D_h = 12.7 mm
Chang and Pan [96]	N_{sub} vs N_{pch}	– Parallel micro-channel heat sink – Horizontal flow	Water	Rectangular: W_{ch} = 99.4 μm H_{ch} = 76.3 μm D_h = 86.3 μm
Flow condensation regime map				
Kim and Mudawar [97]	We^* vs X_{tt}	– Parallel micro-channel heat sink – horizontal flow	FC-72	Rectangular: D_h = 1.0 mm

Table 4
Parameters employed in flow regime maps.

Parameter	Description
Force balance/mass flow related	
$j_f = \frac{G(1-x_e)}{\rho_f}$	Superficial liquid velocity [91,98]
$j_f = \frac{Gx_e}{\rho_f}$	Superficial vapor velocity [91,98]
$j_{g,cor} = \sqrt{\rho_g/\rho_{air}}\, j_g$	Vapor superficial velocity corrected relative to air [99,100]
$Re_f = \frac{(1-x)GD_h}{\mu_f}$	Liquid Reynolds number [101]
$Re_g = \frac{xGD_h}{\mu_g}$	Vapor Reynolds number [101]
$Su_k = \frac{\rho_k \sigma D_h}{\mu_k^2}$	Suratman number [101]
We^*	Modified Weber number [101]
Phase change/heat flux related	
$Bo = \frac{q''_H}{Gh_{fg}}$	Boiling number
$Ja^* = \left(\frac{c_{pf}\Delta T_{sub,in}}{h_{fg}}\right)$	Modified Jacob number
$N_{pch} = Bo\left(\frac{L_{ch}}{D_h}\right)\left(\frac{\rho_f-\rho_g}{\rho_g}\right)$	Phase change number [95]
$N_{sub} = \left(\frac{\rho_f-\rho_g}{\rho_g}\right)\frac{h_{sub,in}}{h_{fg}}$	Subcooling number [95]
$q^* = \frac{q''_B}{G h_{sub,in}}\frac{T_{w,max}}{T_{w,avg}}$	Dimensionless heat flux (accounts for subcooling and temperature distribution effects) [88]
$X_{tt} = \left(\frac{\mu_f}{\mu_g}\right)^{0.1}\left(\frac{1-x}{x}\right)^{0.9}\left(\frac{\nu_f}{\nu_g}\right)^{0.5}$	Turbulent-turbulent Lockhart-Martinelli parameter [102,103]

Notice that the boundary $X_{tt} \leq 1$ can be also expressed as

$$x_e \geqslant \left[1 + \left(\frac{\mu_g}{\mu_f}\right)^{1/9}\left(\frac{\nu_g}{\nu_f}\right)^{5/9}\right]^{-1}. \quad (21)$$

One limitation of Fig. 12(b) is that it does not explicitly distinguish dryout boundaries. Fig. 12(c) provides an alternative means for segregating dryout from non-dryout data. It shows the data presented in terms of vapor Reynolds number as function of the phase change number N_{pch} (defined in Table 4) and suggests dryout commences above a vapor Reynolds number boundary given by

$$Re_g \geqslant 13,470 - 310N_{pch}, \quad (22)$$

Overall, the combination of regime maps in Fig. 12(b) and (c) provides a comprehensive means for predicting both dominant transient flow regimes and dryout conditions.

3.2.3. Local heat transfer coefficient trends

Heat flux and mass velocity are the primary parameters examined in this study that dictate both dominant heat transfer mechanisms and magnitude of the local two-phase heat transfer coefficient. Fig. 13(a) shows the variation of h with x_e for G = 170.83 kg/m^2 s and different values of base heat flux. Within the saturated boiling region ($x_e > 0$), increasing the heat flux causes appreciable and monotonic increases in h for qualities up to x_e = 0.5, which can be defined loosely as the upper limit for the nucleate boiling dominant region of the channel. Notice that h shows a stronger response to heat flux variations for $x_e \leq 0.3$, where the bubbly/slug flow is observed and nucleate boiling is strongest. The dependence of h on heat flux weakens between x_e = 0.3 and 0.5 as bubble nucleation subsided and discrete bubbles coalesce into elongated bubbles, signaling transition to slug flow. Around x_e = 0.5, significant liquid slug breakup begins to take effect as the flow transitions from slug to annular. Here, h shows both very

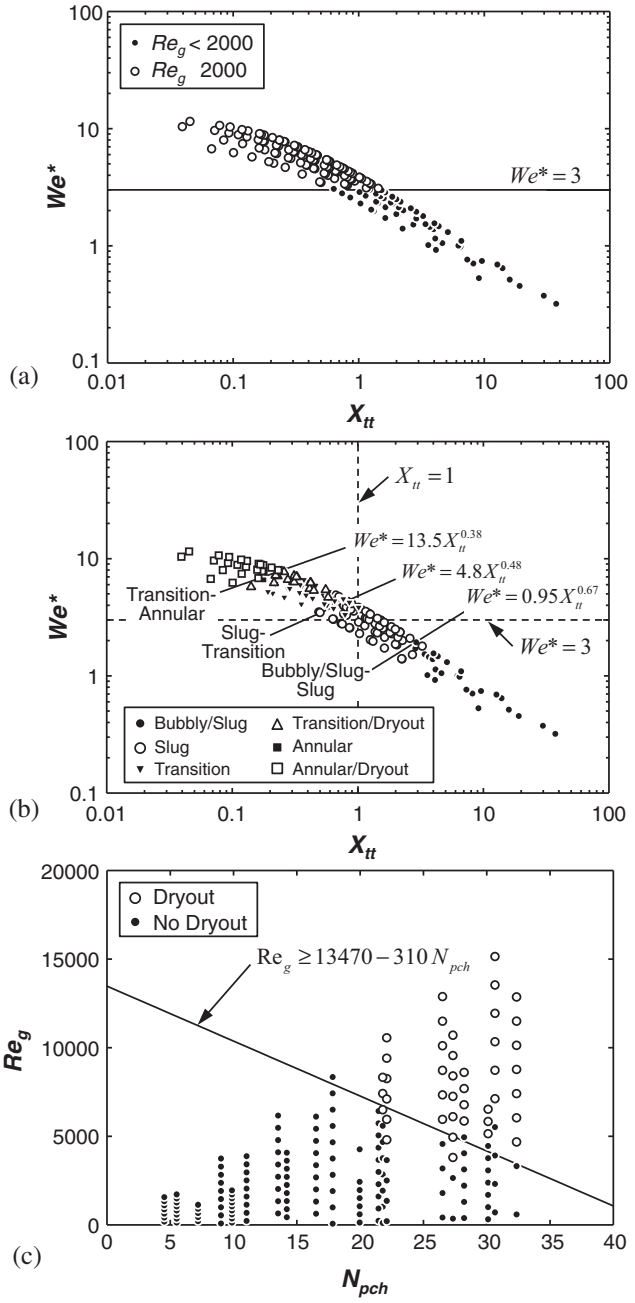

Fig. 12. Transient flow regimes transitions: (a) We^* versus X_{tt} for laminar and turbulent vapor Reynolds numbers, (b) new We^* versus X_{tt} regime map, and (c) Re_g versus N_{pch} dryout boundary map.

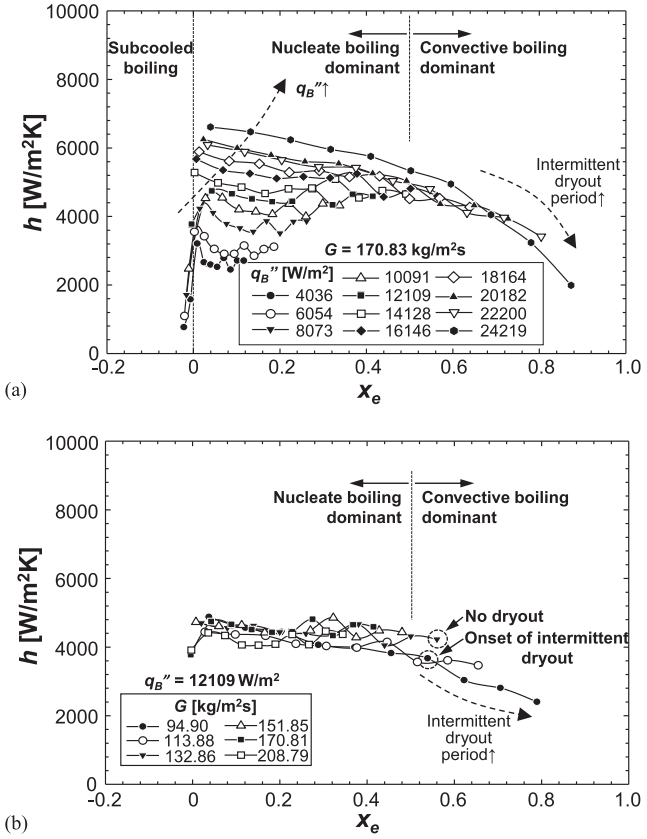

Fig. 13. Variations of local heat transfer coefficient with quality for (a) G = 170.83 kg/m^2 s and different heat fluxes, and (b) q_B'' = 12,109 W/m^2 and different mass velocities.

weak dependence on heat flux and appreciable decline with increasing x_e as nucleation is fully suppressed and the heat transfer mechanism switches from mostly nucleate boiling dominant to convective boiling dominant. Three reasons have been suggested in the literature for the gradual decrease in h with increasing x_e: (a) reduction in the momentum of liquid waves [65], (b) incipient dryout in the annular film resulting from high vapor shear [64,104], and (c) increasing period of intermittent dryout [64]. Notice, for the highest heat flux of q_B'' = 24,219 W/m^2, the sharp reduction in h starting at x_e = 0.5. This trend is consistent with intermittent dryout, which is the mechanism responsible for heat transfer degradation at high heat fluxes [45,64], with more sustained intermittent dryout with increasing x_e culminating in a substantial decrease in h.

Fig. 13(b) shows the variation of h with x_e for q_B'' = 12,109 W/m^2 and different values of mass velocity. In the nucleate boiling dominant region corresponding to x_e < 0.5, h shows both weak and non-monotonic dependence on G. For the convective boiling region corresponding to x_e > 0.5, intermittent dryout is initiated around x_e = 0.54 and z = 391.67 mm for the lowest mass velocity of G = 94.90 kg/m^2 s, but delayed towards the end of the channel, z = 565.40 mm, for G = 132.86 kg/m^2 s, where x_e = 0.56.

Fig. 14(a) and (b) provide video evidence of the dominant mechanisms just discussed. Fig. 14(a) shows representative images of the liquid deficient period (t_1) and surge period (t_2) corresponding to the highest flux condition of q_B'' = 24,219 W/m^2 and G = 170.83 kg/m^2 s in Fig. 13(a) that displayed a large decline in h at high x_e due to dryout. The initial decrease in the heat transfer coefficient from the inlet to z = 160.02 mm is attributed to suppression of nucleate boiling during the liquid surge period (t_2). But in the liquid deficient period (t_1), incipient dryout is observed starting around z = 217.93 mm; this is where the film becomes susceptible to localized dryout. The liquid film is momentarily completely evaporated during the liquid deficient period starting around z = 333.76 mm, marking the onset of intermittent dryout. Accompanying the film evaporation is a sharp decrease in the heat transfer coefficient as shown earlier in Fig. 13(a). Thereafter, short, broken liquid films are observed, and the dryout period increases as the amount of liquid decreases towards the end of the channel (z = 565.40 mm), which is indicated by the high quality of x_e = 0.874 at that location.

Fig. 14(b) shows, for two adjacent channels, representative images of the liquid deficient period (t_1) and liquid surge period (t_2) for q_B'' = 12,109 W/m^2 and G = 94.90 and 132.86 kg/m^2 s, the

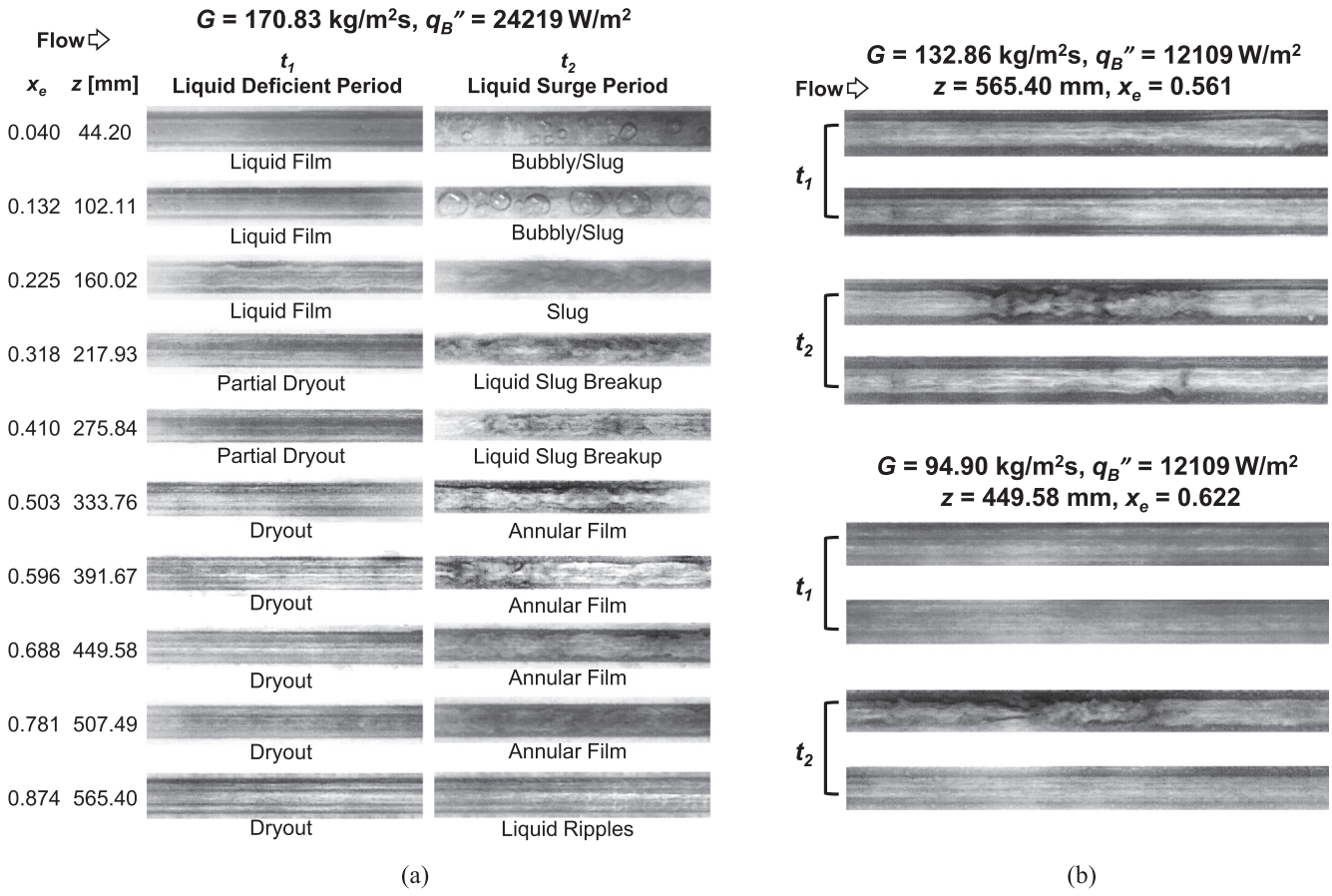

Fig. 14. Images of saturated flow boiling in two adjacent channels for different operating conditions. (a) Flow regime variations along the micro-channels during the liquid deficient period and the liquid surge period for $G = 170.83$ kg/m^2 s and $q_B'' = 24{,}219$ W/m^2. (b) Initiation of intermittent dryout at $q_B'' = 12{,}109$ W/m^2 and $G = 132.86$ and 94.90 kg/m^2 s.

two conditions discussed earlier in conjunction with Fig. 13(b). Notice how the sharp decline in h due to intermittent dryout is observed for $G = 94.90$ kg/m^2 s, but not the higher mass velocity.

3.2.4. Correlation of heat transfer coefficient data

A recent study by the present authors [64] included an extensive assessment of the accuracy of eight prior saturated boiling correlations [69,105–111], some originally developed for macro-channels and the others for micro-channels. The assessment was based on the average two-phase heat transfer coefficient, and the data was for the same micro-channel module used in the present study as well as a shorter module, and same working fluid. However, the micro-channel module in the previous study was incorporated as an evaporator in a vapor compression loop instead of the pumped loop used in the present study. Of the eight correlations, only the one by Kim and Mudawar [111] yielded acceptable predictions in both accuracy and trend, evidenced by a MAE of 21.19%, with $\theta = 69.92\%$ and $\zeta = 95.12\%$ of the predictions falling within ±30% and ±50% of the data, respectively, as shown in Fig. 15(a). Notice that also included in the same figure are data for a shorter micro-channel module ($L = 152.4$ mm) containing 75 parallel micro-channels having the same cross-section as the module used in the present study. The superior performance of the Kim and Mudawar correlation was attributed to its 'universal' formulation, being constructed from a massive database of 10,805 mini/micro-channel flow boiling data points amassed from 31 different sources. The database consists of 18 working fluids, hydraulic diameters of 0.19–6.5 mm, mass velocities of 19–1608 kg/m^2 s, liquid-only Reynolds numbers of 57–49,820, qualities of 0–1, and reduced pressures of 0.005–0.69. The Kim and Mudawar correlation covers both the nucleate boiling and convective boiling regions of saturated boiling, and is valid for both single channels and multi-channel heat sinks. This correlation is one of several universal correlations recently developed by Kim and Mudawar to predict two-phase pressure drop in two-phase adiabatic and condensing flows [112] and in flow boiling [113], as well as heat transfer in both flow boiling [111] and flow condensation [114]. Since it is not a goal of the present study to repeat the assessment of prior correlations, only the universal correlation of Kim and Mudawar is examined against the present data.

The present study yielded 655 data points for the local saturated boiling heat transfer coefficient spanning the ranges of $G = 75.9$–208.8 kg/m^2 s and $q_B'' = 4036$–$28{,}255$ W/m^2. Fig. 15(b) shows the universal correlation of Kim and Mudawar yields fair accuracy in predicting the present data, which indicated by a MAE of 36.46%, with $\theta = 23.36\%$ and $\zeta = 91.15\%$. The accuracy achieved here is inferior to that achieved by the present authors [64] for the same test module and same working fluid, with the test module inserted into a vapor compressions loop instead of the pumped loop used in the present study.

To better explain these differences in predictive accuracy, the MAE is segregated further based on the observed transient flow regimes. Of the present 655 data points, 116, 229, 171, 61, and 77 are associated with the bubbly/slug, slug, transition, transition/intermittent dryout, and annular/intermittent dryout flow regimes, respectively. Fig. 15(c) shows predictive accuracy is compromised mostly in the upstream bubbly/slug and slug regimes, which are dominated by nucleate boiling, but the accuracy

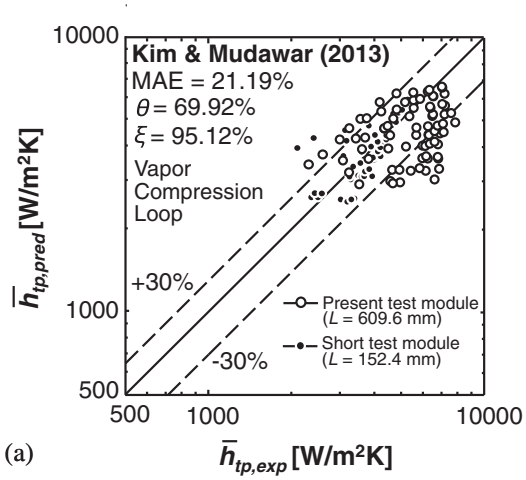

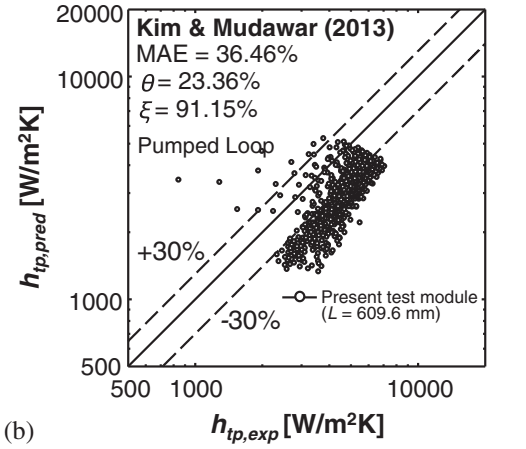

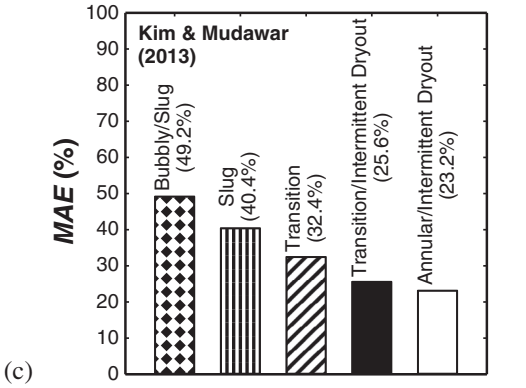

Fig. 15. (a) Comparison of average heat transfer coefficient data obtained by authors [64] using a vapor compression loop with predictions of the universal correlation of Kim and Mudawar [111]. (b) Comparison of present local heat transfer coefficient data obtained using a pumped loop with predictions of the Kim and Mudawar correlation. (c) MAE for the data in (b) segregated relative to different transient flow regimes.

improves significantly for the downstream transition, transition/intermittent dryout, and annular/intermittent dryout regimes, which are dominated by convective boiling. While better overall predictive accuracy can be achieved by modifying the nucleate boiling portion of the correlation, the high predictive accuracy of this correlation against many fluids and over broad ranges of operating conditions indicates such an attempt is unwarranted at the present time, especially that additional data with the present test module will be acquired in the foreseeable future.

4. Conclusions

This study explored variations of the local heat transfer coefficient for R-134a along a test module containing 100 of 1×1 mm^2 square micro-channels. The large length of the micro-channels used (609.6 mm) produced broad axial variations in flow regimes and associated heat transfer mechanisms. With the fluid entering the test module in subcooled state, it was possible to capture both the subcooled boiling ($x_e < 0$) and saturated boiling ($x_e > 0$) regions with great detail. Using a combination of temperature measurements along the heat sink and high-speed video motion analysis of the interfacial behavior, it was possible to explore crucial details of the flow, including dominant flow regimes, flow instabilities, and downstream dryout effects. Key findings from the study can be summarized as follows:

(1) Two sub-regions of the subcooled boiling region, partially developed boiling (PDB) and fully developed boiling (FDB), were identified and examined relative to dominant interfacial and heat transfer mechanisms. The upstream PDB region features small bubbles that fail to grow as they travel along the channel because of strong condensation in the highly subcooled bulk flow. On the other hand, axial warming of the bulk flow in the FDB region allows bubbles to both grow and coalesce with one another. Flow oscillations cause some overlap between the PDB and FDB regions. Among several previous correlations for subcooled boiling, a correlation by Moles and Shaw [86] shows the best accuracy (MAE = 13.62%) in predicting the present PDB and FDB data.

(2) Unlike macro-channel flows, where flow regimes can be clearly demarcated, the flow regimes in micro-channels are associated with transient fluctuations that are caused by flow instabilities, especially vapor backflow to the inlet plenum. The dominant flow behavior and associated dryout effects are successfully characterized with the aid of a new transient flow regime map and a dryout map, respectively.

(3) Examination of local heat transfer coefficient data in the saturated boiling region points to the existence of three separate regions: nucleate boiling dominated region for $x_e < 0.3$, region of combined nucleate and convective boiling for $0.3 < x_e < 0.5$, and convective boiling dominated region for $x_e > 0.5$. Within the latter, the local heat transfer coefficient incurs a gradual decrease after the point of incipient dryout, followed by a sharp decrease downstream because of intermittent dryout. The recent universal correlation of Kim and Mudawar's [111] provides fair accuracy in predicting the saturated boiling heat transfer data, though better accuracy is achieved in the convective boiling region as compared to the nucleate boiling region.

Conflict of interest

The author declares that there is no conflict of interest

Acknowledgement

The authors are grateful for the support of the National Aeronautics and Space Administration (NASA) under grant NNX17AK98G.

Appendix A. Supplementary material

Supplementary data associated with this article can be found, in the online version, at https://doi.org/10.1016/j.ijheatmasstransfer.2018.02.020.

References

[1] I. Mudawar, Assessment of high-heat-flux thermal management schemes, IEEE Trans. - CPMT 24 (2001) 122–141.
[2] C.L. Tien, K.S. Chung, Entrainment limits in heat pipes, AIAA J. 17 (1979) 643–646.
[3] T.J. LaClair, I. Mudawar, Thermal transients in a capillary evaporator prior to the initiation of boiling, Int. J. Heat Mass Transf. 43 (2000) 3937–3952.
[4] M. Shafahi, V. Bianco, H. Vafai, O. Manco, An investigation of the thermal performance of cylindrical heat pipes using nanofluids, Int. J. Heat Mass Transf. 53 (2010) 376–383.
[5] P.J. Marto, V.J. Lepere, Pool boiling heat transfer from enhanced surfaces to dielectric fluids, J. Heat Transf. 104 (1982) 292–299.
[6] I. Mudawar, T.M. Anderson, Parametric investigation into the effects of pressure, subcooling, surface augmentation and choice of coolant on pool boiling in the design of cooling systems for high-power density chips, J. Electron. Pack. 112 (1990) 375–382.
[7] I. Mudawar, T.M. Anderson, Optimization of extended surfaces for high flux chip cooling by pool boiling, J. Electron. Pack. 115 (1993) 89–100.
[8] J.A. Shmerler, I. Mudawar, Local heat transfer coefficient in wavy free-falling turbulent liquid films undergoing uniform sensible heating, Int. J. Heat Mass Transf. 31 (1988) 67–77.
[9] I. Mudawar, R.A. Houpt, R.A., Mass and momentum transport in smooth falling liquid films laminarized at relatively high Reynolds numbers, Int. J. Heat Mass Transf. 36 (1993) 3437–3448.
[10] C.O. Gersey, I. Mudawar, Effects of heater length and orientation on the trigger mechanism for near-saturated flow boiling CHF - I. Photographic and statistical characterization of the near-wall interfacial features, Int. J. Heat Mass Transf. 38 (1995) 629–642.
[11] S.M. Ghiaasiaan, Two-phase Flow, Boiling and Condensation in Conventional and Miniature Systems, Cambridge University Press, New York, 2008.
[12] W. Qu, I. Mudawar, Thermal design methodology for high-heat-flux single-phase and two-phase micro-channel heat sinks, in: Proc. I-THERM 2002, San Diego, California, pp. 347–359.
[13] J.Y. Min, S.P. Jang, S.J. Kim, Effect of tip clearance on the cooling performance of a microchannel heat sink, Int. J. Heat Mass Transf. 47 (2004) 1099–1103.
[14] J. Lee, I. Mudawar, Critical heat flux for subcooled flow boiling in micro-channel heat sinks, Int. J. Heat Mass Transf. 52 (2009) 3341–3352.
[15] J. Lee, I. Mudawar, Fluid flow and heat transfer characteristics of low temperature two-phase micro-channel heat sinks – part 1: experimental methods and flow visualization results, Int. J. Heat Mass Transf. 51 (2008) 4315–4326.
[16] M. Monde, T. Inoue, Critical heat flux in saturated forced convective boiling on a heated disk with multiple impinging jets, J. Heat Transf. 113 (1991) 722–727.
[17] D.C. Wadsworth, I. Mudawar, Enhancement of single-phase heat transfer and critical heat flux from an ultra-high-flux simulated microelectronic heat source to a rectangular impinging jet of dielectric liquid, J. Heat Transf. 114 (1992) 764–768.
[18] M.E. Johns, I. Mudawar, An ultra-high power two-phase jet-impingement avionic clamshell module, J. Electronic Pack. 118 (1996) 264–270.
[19] I. Mudawar, Recent advances in high-flux, two-phase thermal management, J. Therm. Sci. Eng. Appl. 5 (2013) 021012.
[20] W.P. Klinzing, J.C. Rozzi, I. Mudawar, Film and transition boiling correlations for quenching of hot surfaces with water sprays, J. Heat Treat. 9 (1992) 91–103.
[21] D.D. Hall, I. Mudawar, Experimental and numerical study of quenching complex-shaped metallic alloys with multiple, overlapping sprays, Int. J. Heat Mass Transf. 38 (1995) 1201–1216.
[22] L. Lin, R. Ponnappan, Heat transfer characteristics of spray cooling in a closed loop, Int. J. Heat Mass Transf. 46 (2003) 3737–3746.
[23] J.D. Bernardin, I. Mudawar, A Leidenfrost point model for impinging droplets and sprays, J. Heat Transf. 126 (2004) 272–278.
[24] M. Visaria, I. Mudawar, Effects of high subcooling on two-phase spray cooling and critical heat flux, Int. J. Heat Mass Transf. 51 (2008) 5269–5278.
[25] I. Mudawar, D. Bharathan, K. Kelly, S. Narumanchi, Two-phase spray cooling of hybrid vehicle electronics, IEEE Trans. – CPMT 32 (2009) 501–512.
[26] M. Visaria, I. Mudawar, Application of two-phase spray cooling for thermal management of electronic devices, IEEE Trans. – CPMT 32 (2009) 784–793.
[27] I. Mudawar, Two-phase micro-channel heat sinks: theory, applications and limitations, J. Electronic Pack. 133 (2011) 041002–41012.
[28] S. Mukherjee, I. Mudawar, Smart pumpless loop for micro-channel electronic cooling using flat and enhanced surfaces, IEEE Trans. – CPMT 26 (2003) 99–109.
[29] S. Mukherjee, I. Mudawar, Pumpless loop for narrow channel and micro-channel boiling from vertical surfaces, J. Electronic Pack. 125 (2003) 431–441.
[30] M.K. Sung, I. Mudawar, Experimental and numerical investigation of single-phase heat transfer using a hybrid jet impingement/micro-channel cooling scheme, Int. J. Heat Mass Transf. 49 (2006) 682–694.
[31] M.K. Sung, I. Mudawar, Single-phase hybrid micro-channel/jet impingement cooling, Int. J. Heat Mass Transf. 51 (2008) 4342–4352.
[32] M.K. Sung, I. Mudawar, Single-phase and two-phase heat transfer characteristics of low temperature hybrid micro-channel/micro-jet impingement cooling module, Int. J. Heat Mass Transf. 51 (2008) 3882–3895.
[33] S.M. Kim, I. Mudawar, Review of two-phase critical flow models and investigation of the relationship between choking, premature CHF, and CHF in micro-channel heat sinks, Int. J. Heat Mass Transf. 87 (2015) 497–511.
[34] M.B. Bowers, I. Mudawar, Two-phase electronic cooling using mini-channel and micro-channel heat sinks - part 2. Flow rate and pressure drop constraints, J. Electronic Pack. 116 (1994) 298–305.
[35] W. Qu, I. Mudawar, Measurement and prediction of pressure drop in two-phase micro-channel heat sinks, J. Heat Mass Transf. 46 (2003) 2737–2753.
[36] G.B. Ganapathi, G. Birur, G. Tsuyuki, R. Krylo, Mars Exploration Rover heat Rejection System Performance – Comparison of Ground and Flight Data, SAE Paper 2004-01-2413, 2004.
[37] G.B. Ganapathi, G. Birur, E. Sunada, J. Miller, Two Phase vs. Single Phase Thermal Loop Trades for Exploration Mission LAT II Architecture, SAE Paper 2008-01-1958, 2008.
[38] F.P. Chiaramonte, J.A. Joshi, Workshop on Critical Issues in Microgravity Fluids, Transport, and Reaction Processes in Advanced Human Support Technology - Final Report, NASA Report TM-2004-212940, Washington, D. C., 2004.
[39] National Research Council, Recapturing a Future for Space Exploration: Life and Physical Sciences Research for a New Era, The National Academies Press, Washington, D.C., 2011.
[40] H. Zhang, I. Mudawar, M.M. Hasan, Experimental assessment of the effects of body force, surface tension force, and inertia on flow boiling CHF, Int. J. Heat Mass Transf. 45 (2002) 4079–4095.
[41] H. Zhang, I. Mudawar, M.M. Hasan, Experimental and theoretical study of orientation effects on flow boiling CHF, Int. J. Heat Mass Transf. 45 (2002) 4463–4478.
[42] H. Zhang, I. Mudawar, M.M. Hasan, Flow boiling CHF in microgravity, Int. J. Heat Mass Transf. 48 (2005) 3107–3118.
[43] C. Konishi, I. Mudawar, Review of flow boiling and critical heat flux in microgravity, Int. J. Heat Mass Transf. 80 (2015) 469–493.
[44] S.H. Lee, I. Mudawar, M.M. Hasan, Thermal analysis of hybrid single-phase, two-phase and heat pump thermal control system (TCS) for future spacecraft, Appl. Therm. Eng. 100 (2016) 190–214.
[45] S. Lin, P.A. Kew, K. Cornwell, Two-phase heat transfer to a refrigerant in a 1 mm diameter tube, Int. J. Refrig. 24 (2001) 51–56.
[46] S. In, S. Jeong, Flow boiling heat transfer characteristics of R123 and R134a in a micro-channel, Int. J. Multiphase Flow 35 (2009) 987–1000.
[47] C.B. Tibiriçá, G. Ribatski, Flow boiling heat transfer of R134a and R245fa in a 2.3 mm tube, Int. J. Heat Mass Transf. 53 (2010) 2459–2468.
[48] M. Ducoulombier, S. Colasson, J. Bonjour, P. Haberschill, Carbon dioxide flow boiling in a single microchannel - Part II: heat transfer, Exp. Therm. Fluid Sci. 35 (2011) 597–611.
[49] L. Wojtan, T. Ursenbacher, J.R. Thome, Investigation of flow boiling in horizontal tubes: Part I - a new diabatic two-phase flow pattern map, Int. J. Heat Mass Transf. 48 (2005) 2955–2969.
[50] R. Revellin, J.R. Thome, A new type of diabatic flow pattern map for boiling heat transfer in microchannels, J. Micromech. Microeng. 17 (2007) 788–796.
[51] Y. Hsu, R.W. Graham, An Analytical and Experimental Study of the Thermal Boundary Layer and Ebullition Cycle in Nucleate Boiling, NASA TN D-594, 1961.
[52] Y.Y. Hsu, On the size range of active nucleation cavities on a heating surface, Trans. ASME J. Heat Transf. 84 (1962) 207–213.
[53] T. Sato, H. Matsumura, On the conditions of incipient subcooled-boiling with forced convection, Bull. JSME 7 (1963) 392–398.
[54] E.J. Davis, G.H. Anderson, The incipience of nucleate boiling in forced convection flow, AIChE J. 12 (1966) 774–780.
[55] A.E. Bergles, W.M. Rohsenow, The determination of forced-convection surface-boiling heat transfer, Trans. ASME J. Heat Transf. Series C 86 (1964) 365–372.
[56] W. Qu, I. Mudawar, Prediction and measurement of incipient boiling heat flux in micro-channel heat sinks, Int. J. Heat Mass Transf. 45 (2002) 3933–3945.
[57] X.F. Peng, H.Y. Hu, B.X. Wang, Boiling nucleation during liquid flow in microchannels, Int. J. Heat Mass Transf. 41 (1998) 101–106.
[58] C. Martín-Callizo, B. Palm, W. Owhaib, Subcooled flow boiling of R-134a in vertical channels of small diameter, Int. J. Multiphase Flow 33 (2007) 822–832.
[59] W.M. Rohsenow, Heat transfer with evaporation, in: Proc. Heat Transfer Symposium, University of Michigan Press, 1953, pp. 101–150.
[60] R.W. Bowring, Physical model based on bubble detachment and calculation of steam voidage in the subcooled region of a heated channel, OECD Halden Reactor Project Report HPR-10, 1962.
[61] M.M. Shah, A general correlation for heat transfer during subcooled boiling in pipes and annuli,, ASHRAE Trans. 83 (Part 1) (1977) 205–217.
[62] S.G. Kandlikar, Heat transfer characteristics in partial boiling, fully developed boiling, and significant void flow regions of subcooled flow boiling, J. Heat Transf. 120 (1998) 395–401.
[63] J. Lee, I. Mudawar, Fluid flow and heat transfer characteristics of low temperature two-phase micro-channel heat sinks – Part 2. Subcooled boiling pressure drop and heat transfer, Int. J. Heat Mass Transf. 51 (2008) 4327–4341.
[64] S. Lee, I. Mudawar, Investigation of flow boiling in large micro-channel heat exchangers in a refrigeration loop for space applications, Int. J. Heat Mass Transf. 97 (2016) 110–129.
[65] S. Lee, I. Mudawar, Transient characteristics of flow boiling in large micro-channel heat exchangers, Int. J. Heat Mass Transf. 103 (2016) 186–202.

[66] S. Saisorn, J. Kaew-On, S. Wongwises, Flow pattern and heat transfer characteristics of R-134a refrigerant during flow boiling in a horizontal circular mini-channel, Int. J. Heat Mass Transf. 53 (2010) 4023–4038.
[67] W. Qu, I. Mudawar, Flow boiling heat transfer in two-phase micro-channel heat sinks––I. Experimental investigation and assessment of correlation methods, Int. J. Heat Mass Transf. 46 (2003) 2755–2771.
[68] W. Qu, I. Mudawar, Flow boiling heat transfer in two-phase micro-channel heat sinks––II. Annular two-phase flow model, Int. J. Heat Mass Transf. 46 (2003) 2773–2784.
[69] J. Lee, I. Mudawar, Two-phase flow in high-heat-flux micro-channel heat sink for refrigeration cooling applications: Part II—heat transfer characteristics, Int. J. Heat Mass Transf. 48 (2005) 941–955.
[70] B. Agostini, J.R. Thome, M. Fabbri, B. Michel, D. Calmi, U. Kloter, High heat flux flow boiling in silicon multi-microchannels – Part I: heat transfer characteristics of refrigerant R236fa, Int. J. Heat Mass Transf. 51 (2008) 5400–5414.
[71] W. Qu, I. Mudawar, Transport phenomena in two-phase micro-channel heat sinks, J. Electron. Pack. 126 (2004) 213–224.
[72] W. Qu, I. Mudawar, Measurement and correlation of critical heat flux in two-phase micro-channel heat sinks, Int. J. Heat Mass Transf. 47 (2004) 2045–2059.
[73] S. Lee, V.S. Devahdhanush, I. Mudawar, Frequency analysis of pressure oscillations in large length-to-diameter two-phase micro-channel heat sinks, Int. J. Heat Mass Transf. 116 (2018) 273–291.
[74] J. Lee, I. Mudawar, Two-phase flow in high-heat-flux micro-channel heat sink for refrigeration cooling applications: Part I––pressure drop characteristics, Int. J. Heat Mass Transf. 48 (2005) 928–940.
[75] J. Lee, I. Mudawar, Implementation of microchannel evaporator for high-heat-flux refrigeration cooling applications, J. Electron. Pack. 128 (2005) 30–37.
[76] S. Lee, V.S. Devahdhanush, I. Mudawar, Pressure drop characteristics of large length-to-diameter two-phase micro-channel heat sinks, Int. J. Heat Mass Transf. 115 (2017) 1258–1275.
[77] K.E. Forster, R. Grief, Heat transfer to a boiling liquid: mechanism and correlations, J. Heat Transf. 81 (1959) 43–53.
[78] T.L. Bergman, F.P. Incropera, A.S. Lavine, D.P. DeWitt, Fundamentals of Heat and Mass Transfer, 7th ed., Wiley and Sons, New York, 2011.
[79] K. Cornwell, P.A. Kew, Boiling in small parallel channels, in: D.P.A. Pilavachi (Ed.), Energy Efficiency in Process Technology, Springer, Netherlands, 1993, pp. 624–638.
[80] F.W. Dittus, L.M.K. Boelter, Heat Transfer in Automobile Radiators of the Tubular Type, vol. 11, University Calif. Pub. Eng., 1930, pp. 443−461.
[81] R.H.S. Winterton, Where did the Dittus and Boelter equation come from?, Int J. Heat Mass Transf. 41 (1998) 809–810.
[82] R.K. Shah, A.L. London, Laminar Flow Forced Convection in Ducts: A Source Book for Compact Heat Exchanger Analytical Data (Supl 1), Academic Press, New York, 1978.
[83] S.S. Papell, Subcooled Boiling Heat Transfer Under Forced Convection in a Heated Tube, NASA Technical Note D-1583, Lewis Research Center, Cleveland, OH, 1963.
[84] A.P. Colburn, A method of correlating forced convection heat transfer data and a comparison with fluid friction, Trans. Am. Inst. Chem. Eng. 29 (1933) 174–210.
[85] M. Badiuzzaman, Correlation of subcooled boiling data, Pak. Eng. 7 (1967) 759–764.
[86] F.D. Moles, J.F.G. Shaw, Boiling heat transfer to subcooled liquids under condition of forced convection, Trans. Inst. Chem. Eng. 50 (1972) 76–84.
[87] E.W. Lemmon, M.L. Huber, M.O. McLinden, Reference Fluid Thermodynamic and Transport Properties – REFPROP Version 8.0, NIST, MD, 2007.
[88] G. Hetsroni, A. Mosyak, Z. Segal, E. Pogrebnyak, Two-phase flow patterns in parallel micro-channels, Int. J. Multiphase Flow 29 (2003) 341–360.
[89] L. Wojtan, T. Ursenbacher, J.R. Thome, Investigation of flow boiling in horizontal tubes: Part I—A new diabatic two-phase flow pattern map, Int. J. Heat Mass Transf. 48 (2005) 2955–2969.
[90] G. Wang, P. Cheng, A.E. Bergles, Effects of inlet/outlet configurations on flow boiling instability in parallel microchannels, Int. J. Heat Mass Transf. 51 (2008) 2267–2281.
[91] K.A. Triplett, S.M. Ghiaasiaan, S.I. Abdel-Khalik, D.L. Sadowski, Gas–liquid two-phase flow in microchannels Part I: two-phase flow patterns, Int. J. Multiphase Flow 25 (1999) 377–394.
[92] A. Kawahara, P.M.-Y. Chung, M. Kawaji, Investigation of two-phase flow pattern, void fraction and pressure drop in a microchannel, Int. J. Multiphase Flow 28 (2002) 1411–1435.
[93] W. Qu, S.-M. Yoon, I. Mudawar, Two-phase flow and heat transfer in rectangular micro-channels, J. Electron. Pack. 126 (2004) 288–300.
[94] I. Hassan, M. Vaillancourt, K. Pehlivan, Two-phase flow regime transitions in microchannels: a comparative experimental study, Microscale Thermophys. Eng. 9 (2005) 165–182.
[95] P. Saha, M. Ishii, N. Zuber, An experimental investigation of the thermally induced flow oscillations in two-phase systems, J. Heat Transf. 98 (1976) 616–622.
[96] K.H. Chang, C. Pan, Two-phase flow instability for boiling in a microchannel heat sink, Int. J. Heat Mass Transf. 50 (2007) 2078–2088.
[97] S.-M. Kim, I. Mudawar, Flow condensation in parallel micro-channels – Part 2: Heat transfer results and correlation technique, Int. J. Heat Mass Transf. 55 (2012) 984–994.
[98] J.M. Mandhane, G.A. Gregory, K. Aziz, A flow pattern map for gas—liquid flow in horizontal pipes, Int. J. Multiphase Flow 1 (1974) 537–553.
[99] M.K. Dobson, J.C. Chato, Condensation in smooth horizontal tubes, J. Heat Transf. 120 (1998) 193–213.
[100] A. Cavallini, G. Censi, D.D. Col, L. Doretti, G.A. Longo, L. Rossetto, Condensation of halogenated refrigerants inside smooth tubes, HVAC&R Res. 8 (2002) 429–451.
[101] H.M. Soliman, Correlation of mist-to-annular transition during condensation, Can. J. Chem. Eng. 61 (1983) 178–182.
[102] H.M. Soliman, The mist-annular transition during condensation and its influence on the heat transfer mechanism, Int. J. Multiphase Flow 12 (1986) 277–288.
[103] Q. Chen, R.S. Amano, M. Xin, Experimental study of flow patterns and regimes of condensation in horizontal three-dimensional micro-fin tubes, Heat Mass Transf. 43 (2006) 201–206.
[104] S.-M. Kim, I. Mudawar, Universal approach to predicting saturated flow boiling heat transfer in mini/micro-channels – Part I. Dryout incipience quality, Int. J. Heat Mass Transf. 64 (2013) 1226–1238.
[105] J.C. Chen, Correlation for boiling heat transfer to saturated fluids in convective flow, Ind. Eng. Chem. Proc. Des. Develop. 5 (1966) 322–329.
[106] G.M. Lazarek, S.H. Black, Evaporative heat transfer, pressure drop and critical heat flux in a small vertical tube with R-113, Int. J. Heat Mass Transf. 25 (1982) 945–960.
[107] Z. Liu, R.H.S. Winterton, A general correlation for saturated and subcooled flow boiling in tubes and annuli, based on a nucleate pool boiling equation, Int. J. Heat Mass Transf. 34 (1991) 2759–2766.
[108] T.N. Tran, M.W. Wambsganss, D.M. France, Small circular- and rectangular-channel boiling with two refrigerants, Int. J. Multiphase Flow 22 (1996) 485–498.
[109] S.G. Kandlikar, P. Balasubramanian, An extension of the flow boiling correlation to transition, laminar, and deep laminar flows in minichannels and microchannels, Heat Transf. Eng. 25 (2004) 86–93.
[110] S.S. Bertsch, E.A. Groll, S.V. Garimella, A composite heat transfer correlation for saturated flow boiling in small channels, Int. J. Heat Mass Transf. 52 (2009) 2110–2118.
[111] S.-M. Kim, I. Mudawar, Universal approach to predicting saturated flow boiling heat transfer in mini/micro-channels – Part II. Two-phase heat transfer coefficient, Int. J. Heat Mass Transf. 64 (2013) 1239–1256.
[112] S.-M. Kim, I. Mudawar, Universal approach to predicting two-phase frictional pressure drop for adiabatic and condensing mini/micro-channel flows, Int. J. Heat Mass Transf. 55 (2012) 3246–3261.
[113] S.-M. Kim, I. Mudawar, Universal approach to predicting two-phase frictional pressure drop for mini/micro-channel saturated flow boiling, Int. J. Heat Mass Transf. 58 (2013) 718–734.
[114] S.-M. Kim, I. Mudawar, Universal approach to predicting heat transfer coefficient for condensing mini/micro-channel flows, Int. J. Heat Mass Transf. 56 (2013) 238–250.